F-actin buckling coordinates contractility and severing in a biomimetic actomyosin cortex

Michael P. Murrell[a] and Margaret L. Gardel[a,b,1]

[a]Institute for Biophysical Dynamics, James Franck Institute, and [b]Department of Physics, University of Chicago, Chicago, IL 60637

Edited by Thomas D. Pollard, Yale University, New Haven, CT, and approved November 2, 2012 (received for review August 28, 2012)

Here we develop a minimal model of the cell actomyosin cortex by forming a quasi-2D cross-linked filamentous actin (F-actin) network adhered to a model cell membrane and contracted by myosin thick filaments. Myosin motors generate both compressive and tensile stresses on F-actin and consequently induce large bending fluctuations, which reduces their effective persistence length to <1 μm. Over a large range of conditions, we show the extent of network contraction corresponds exactly to the extent of individual F-actin shortening via buckling. This demonstrates an essential role of buckling in breaking the symmetry between tensile and compressive stresses to facilitate mesoscale network contraction of up to 80% strain. Portions of buckled F-actin with a radius of curvature ∼300 nm are prone to severing and thus compressive stresses mechanically coordinate contractility with F-actin severing, the initial step of F-actin turnover. Finally, the F-actin curvature acquired by myosin-induced stresses can be further constrained by adhesion of the network to a membrane, accelerating filament severing but inhibiting the long-range transmission of the stresses necessary for network contractility. Thus, the extent of membrane adhesion can regulate the coupling between network contraction and F-actin severing. These data demonstrate the essential role of the nonlinear response of F-actin to compressive stresses in potentiating both myosin-mediated contractility and filament severing. This may serve as a general mechanism to mechanically coordinate contractility and cortical dynamics across diverse actomyosin assemblies in smooth muscle and nonmuscle cells.

cytoskeleton | active gels | nonequilibrium | myosin II

Changes in cell shape, as required for migration and division, are mediated by the cell cortex, a thin shell of cross-linked actin filaments (F-actin) bound to the inner leaflet of the plasma membrane. The actin cortex is an apolar, disordered network of F-actin decorated with myosin II motors. Myosin II motors drive contractility of the cortical actin network, enabling shape change and cytoplasmic flows underlying diverse physiological processes ranging from cell division and migration to tissue morphogenesis (1–6). Variable coupling of these actomyosin forces to the plasma membrane regulates transmission of stresses to cell–matrix or cell–cell adhesions to modulate cell shape change and force transmission (7–9). Actomyosin stresses are also implicated in driving cortical F-actin filament turnover in vivo to maintain a highly dynamic actin cytoskeleton (2–4). Thus, actin polymerization dynamics and contractile force generation are intimately coupled in the actomyosin cortex.

The actin filaments within the cortex are highly dynamic and constantly turning over, renewing themselves within minutes (10). The initial step of actin cortex turnover involves the severing of F-actin, which both destabilizes existing filaments and releases monomers for de novo polymerization. To date, the predominant mechanism identified for destabilizing F-actin both in vivo and in vitro is severing by ADF/cofilin. Recent data have indicated that the mechanism for severing by cofilin is mechanical in nature, making it prone to spontaneous fragmentation (11). There is mounting evidence that myosin II also plays a role in the turnover of cortical actin (2–4), and myosin II-mediated F-actin disassembly is observed in vitro (12). Given the known role of myosin II in the generation of contractile stresses and its association with F-actin disassembly, these mechanisms are likely related, although no such mechanism has been directly shown.

Myosin II motors generate local stresses at the molecular level within the actin cytoskeleton to drive contractility of the cortex at 10- to 100-μm length and nano-Newton force scales. The mechanisms of force transmission within a disordered actomyosin cortex are not well understood. In the sarcomeric organization of actomyosin found in striated muscle, the relative sliding of myosin against polarity-organized F-actin preferentially generates tensile stresses to drive contraction (13). However, actomyosin networks in nonmuscle cells lack sarcomeric organization (14) and a mechanism to break the symmetry between tensile and compressive stresses is necessary (15). Theoretical work has demonstrated that such symmetry-breaking mechanisms could arise in 2D and 3D networks due to inherent mechanical stability of tensile stresses (16), by myosin II "sorting" of F-actin polarity (17) or spatial regulation of F-actin polymerization (18). The role of the nonlinear elastic response of F-actin in facilitating contraction of bundles (19) and networks (20–22) has also been explored in theory and simulation, and F-actin buckling is observed during contraction of actomyosin bundles (19). However, it is not clear to what extent each of these microscopic mechanisms contributes to contractile deformation of a quasi-2D network at larger length scales. Moreover, mechanisms to mechanically coordinate network contractility with F-actin turnover are not well understood.

Results and Discussion

To identify mechanisms of contractility in disordered actin networks, we developed an in vitro model of the actomyosin cortex reconstituted from a minimal set of components that is amenable to high-resolution imaging of fluorescently tagged constituents. In this model, the crowding agent methylcellulose (MC) is used to localize F-actin to the surface of a supported lipid bilayer (Fig. 1 *A* and *B* and Fig. S1). We use a MC concentration (0.25%) that is sufficient to crowd phalloidin-stabilized F-actin near the surface of the lipid bilayer (Fig. 1 *A* and *B*, Figs. S1 and S2, and Movies S1 and S2), but low enough to prevent significant F-actin bundling (Fig. S3). Nevertheless, MC can induce interactions between F-actin filaments (23) and spatial variation of filament density is observed. The alignment of F-actin we observe during accumulation onto the membrane can be altered by perturbing formation conditions (Movie S3); changes to filament alignment do not impact any of the conclusions of our work, as myosin activity rapidly reorganizes F-actin. To cross-link F-actin into space-spanning networks, we use the flexible cross-linking protein α-actinin (24), which at low concentrations ($R_{\text{xlink}} = 0.003$)

Author contributions: M.P.M. and M.L.G. designed research; M.P.M. performed research; M.P.M. contributed new reagents/analytic tools; M.P.M. analyzed data; and M.P.M. and M.L.G. wrote the paper.

The authors declare no conflict of interest.

This article is a PNAS Direct Submission.

[1]To whom correspondence should be addressed. E-mail: gardel@uchicago.edu.

This article contains supporting information online at www.pnas.org/lookup/suppl/doi:10.1073/pnas.1214753109/-/DCSupplemental.

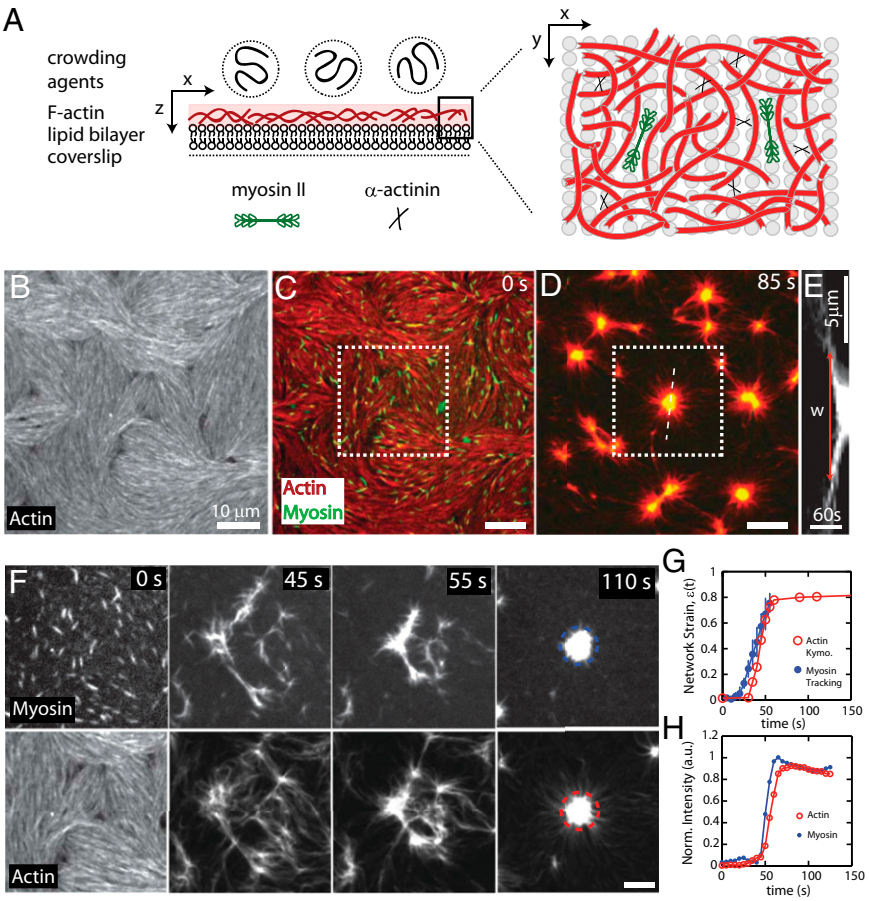

Fig. 1. Reconstitution of a model contractile actomyosin cortex. (*A*) Schematic illustration of reconstituted system. F-actin is crowded to the surface of a supported lipid bilayer (SLB) after which cross-linking proteins and skeletal muscle myosin II filaments are added. Data in *B*–*H* are from 1 μM F-actin (100% labeled) crowded to the surface of 91% EPC/9% nickel-tagged lipid (NTA) (mol/mol) SLB with $R_{xlink} = 0$ and $R_{Adh} = 0$. (*B*) Alexa-568–labeled F-actin at the SLB surface. (*C* and *D*) F-actin (red) and myosin II (green) (*C*) immediately (0 s) after myosin thick filament formation and (*D*) 85 s after myosin filaments assembled ($t = 0$ s). (*E*) Kymograph of the actin over time taken at the white dotted line in *D* with the width of the contractile zone *w* indicated. (*F*) Magnified images of myosin and F-actin from square region indicated in *C* during contraction. Myosin filaments appear at 0 s. (*G*) Contractile strain of the actin network from the kymograph in *E*. (*H*) Average normalized myosin and actin fluorescence intensity within the center of contraction, indicated in *F*.

forms a network of isotropically cross-linked filaments and at high concentrations ($R_{xlink} = 0.03$) forms a network of dense bundles (Fig. S3). Specific adhesion of F-actin to the model membrane is mediated by the incorporation of nickel-tagged (NTA) lipids in the bilayer and the addition of a histidine-tagged actin-binding domain of fimbrin (FimA2) (25) (Fig. S1). Membrane adhesion via FimA2 immobilizes F-actin and prevents filament alignment (Fig. S1, Movie S4, and Fig. 4*A*). Thus, we can create a thin (~200 nm) and dense quasi-2D network of F-actin (Fig. S1) whose cross-linking density (R_{xlink} = [α-actinin]/[G-actin]) and membrane adhesion (R_{Adh} = [FimA2]/[G-actin]) can be controlled precisely.

Upon the addition of skeletal muscle myosin dimers to the sample chamber, myosin thick filaments ~1.5 μm in length and containing ~400 motor domains assemble rapidly (~1–2 min) on the F-actin network (Fig. S4). After assembly, myosin II thick filaments drive rapid motions of F-actin and myosin to form a dynamic and contractile network (Fig. 1 *C*–*E* and Movies S5 and S6). Myosin activity drives the contraction of the F-actin network over a certain length scale into dense foci at rates of 150 nm/s (from kymograph) (Fig. 1 *D*–*F*). Once contracted, these aggregates can undergo further coalescence with each other (22). We quantify compressive strain within the contractile domain by tracking the position of myosin thick filaments and measuring the separation distance between select pairs during contraction, $w(t)$ (Fig. S5). The contractile strain of the network, ε, is then determined by $\varepsilon(t) = 1 - w(t)/w_0$, where w_0 is the initial separation distance. Over the first 60–90 s, the network strain increases from 0 to 80% (Fig. 1*G*) and coincides with a rapid increase in local density of actomyosin into foci (Fig. 1*H* and Fig. S5). After this time, no significant network strain is measured although movement of actomyosin continues to persist for >15 min.

As the network architecture is perturbed by changes to F-actin length, cross-linking density, and strength of membrane adhesion, contraction is qualitatively similar, but the length scale over which it occurs is quantitatively distinct. In the absence of α-actinin, the contractile domain size is similar to the F-actin length and indicates that myosin or putative cross-linking by MC is insufficient to facilitate cross-linking over large distances (Figs. S6 and S7). When a low concentration of α-actinin ($R_{xlink} = 0.003$) is added, the contractile domain size increases and is consistent with enhanced network connectivity (Movie S7 and Fig. S6). When $R_{xlink} = 0.03$, the network of bundled actin filaments contracts as a single domain over millimeter length scales (Movie S8 and Fig. S8). To permit quantification of contraction in these networks of α-actinin/F-actin bundles, we locally activate myosin activity within the field of view to spatially restrict contraction (Movie S9 and Fig. S8). By contrast, adhesion to the membrane via His-FimA2 significantly reduces the contractile domain size to <3 μm (Fig. S6), reflecting an

adhesive drag impeding contraction. Thus, changes to F-actin length, cross-link density, and strength of membrane adhesion strongly modulate the contractile domain size.

To identify microscopic origins of contraction across all these conditions, we image individual F-actin by labeling on 1–2% of the filaments within the quasi-2D network (Fig. 2*A*). Immediately upon the addition of myosin thick filaments, F-actin bending and buckling are observed, with the amplitude and frequency of bends increasing during contraction (Movie S10). F-actin buckling results from compressive stress on F-actin segments and could arise from several mechanisms, including from differences in the rate of myosin sliding along filaments (Fig. 2 *B–D* and Movie S11) or the nature of stress fluctuations within the surrounding network, as has been previously observed for microtubules in actomyosin networks (26). The minimum forces required to drive these curvatures in the absence of adhesion and bundling are determined by the Euler buckling threshold for F-actin and are ~3–4 pN for a radius of curvature $r_c = 300$ nm (27), well within the range of forces generated by myosin II filaments. Filament bending is observed over all conditions, including networks of thick α-actinin–mediated bundles (Fig. S8 and Movie S9) and high membrane adhesion (Fig. 4*B* and Movie S12), although the mean curvatures of bends in these conditions differ. In bundles and high membrane adhesion, large radii of curvature are rarely observed, reflecting constraints of the surrounding environment.

The change in filament curvature during contraction can be quantified by measuring F-actin's effective persistence length over time, $\ell'_p(t)$. At times before and up to myosin addition, the persistence length $\ell'_p(t<0)$ remains constant and is >10 μm, consistent with the known persistence length of F-actin (17 μm) with the increased value presumed to reflect the quasi-2D and crowded environment. Upon myosin addition, ℓ'_p drops rapidly to ~1 μm for both entangled ($R_{xlink} = 0$) and highly bundled ($R_{xlink} = 0.03$) networks as contraction occurs (Fig. 2 *E* and *F* and Fig. S9).

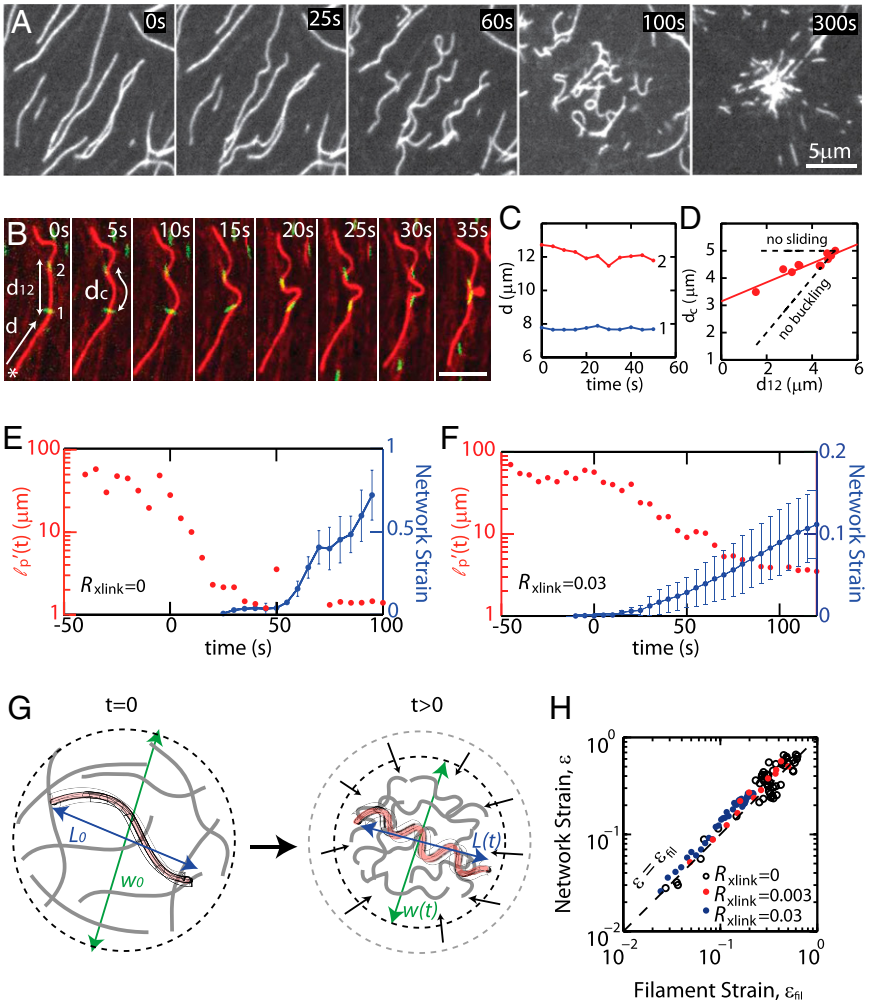

Fig. 2. Myosin-induced F-actin buckling occurs concomitantly with contraction. (*A*) Images of individual F-actin (1–2% labeled) during contraction of sample with $R_{xlink} = 0$ and $R_{Adh} = 0$ (Movie S10). Myosin thick filaments form at 0 s. Data in *B–D* are from sample with $R_{xlink} = 0.003$ and $R_{Adh} = 0$ (Movie S11). (*B*) Myosin (green) translocating along F-actin (red) where *d* is the distance of myosin from F-actin barbed end (*), d_c is length of F-actin between myosin punctae, and d_{12} is the Euclidean distance between myosin thick filaments. (*C*) Distance *d* of myosin punctae from the barbed end of F-actin over time. (*D*) d_c as a function of d_{12}, with dashed lines indicating the results for changes expected due to buckling, with no actomyosin sliding (no sliding), and those for relative sliding, with no F-actin buckling (no buckling). (*E* and *F*) Persistence length, l_p' (red) and network strain (blue) for (*E*) $R_{xlink} = 0$ ($R_{Adh} = 0$) (Movie S10) and (*F*) $R_{xlink} = 0.03$ ($R_{Adh} = 0$) (Movie S9). The l_p' data are for a single F-actin, and the network strain reflects the average of four myosin pairs in *E* and five in *F*, each within a single experiment. (*G*) Schematic indicating measurement of filament compressive strain, determined by tracking changes in end-to-end length of single filaments, and network contractile strain, determined by changes in the size of the network. (*H*) Network strain ε as a function of filament strain ε_{fil} during contraction for $R_{xlink} = 0$, 0.003, and 0.03 ($R_{Adh} = 0$). Dashed line indicates $\varepsilon = \varepsilon_{fil}$. The data are the average of four myosin pairs and nine filaments for $R_{xlink} = 0$, seven myosin pairs and six filaments for $R_{xlink} = 0.003$, and five myosin pairs and seven filaments for $R_{xlink} = 0.03$, each for a single experiment.

The persistence length continues to decrease further during contraction up to strains of 80%. Thus, the generation of large contractile strains in a disordered actin network is associated with compressive stresses that bend and buckle actin filaments.

The origin of network contraction could arise from numerous mechanisms. A sarcomere-like mechanism could arise from tensile stresses driving actomyosin sliding to increase overlap of actin and myosin filaments and, thus, shorten the overall length. Filament buckling is another means to shorten the end-to-end length of F-actin and, in the presence of tensile forces to drive coalescence, could also result in contraction. We measure the filament strain by measuring the fraction change in end-to-end filament length $L(t)$ during contraction, $\varepsilon_{fil} = 1 - L(t)/L_0$, where L_0 is the initial distance between filament ends (Fig. 2*G*), and find that the extent of network contraction corresponds exactly to the extent of filament shortening via buckling such that $\varepsilon = \varepsilon_{fil}$ (Fig. 2*H*). Moreover, this exact matching of filament compressive strain and network contraction is observed over a large range of cross-link concentrations (Fig. 2*H*). If F-actin buckling did not play a significant role in network contraction, we would expect a lack of correlation between these parameters and $\varepsilon < \varepsilon_{fil}$. By contrast, a sarcomere-like sliding contraction mechanism would enable contraction without any changes to filament length, such that $\varepsilon > \varepsilon_{fil}$. Instead, we observe that network contraction occurs concomitantly with filament buckling, suggesting an important role in its regulation.

Filament severing occurs during myosin-mediated bending fluctuations and motions. Severing events predominately localize to sites of high F-actin curvature (>99%) (Fig. 3*A*) with remaining events occurring at apparently taut and straight filament portions (Fig. S10). To explore the connection between F-actin curvature and severing, we measure the radius of curvature, r_c, of F-actin immediately before a severing event (Fig. 3*B*). We find that severing occurs predominately at or below an r_c of ~300 nm, irrespective of the cross-linking density (Fig. 3*B*), and is not a product of photodamage (Movie S13). Moreover, filament severing occurs throughout contraction as myosin-generated stresses continually drive bending fluctuations of filaments (Fig. 3*C*). At the initial stages of contraction, the severing rate is low and large radii of curvature bends facilitate contractility. Severing increases at the later stages of contraction, where small radii of curvature are apparent, and severing events do not contribute significantly to further contraction within the next 10–20 s (Fig. 3*A*). Thus, the compressive stresses arising from myosin motors result in mechanically mediated F-actin severing.

In the cell, the actomyosin cortex is coupled to the plasma membrane by cross-linking and regulatory proteins (28). To explore the consequence of membrane adhesion on actomyosin contraction, we mimic this condition by coupling the actin network to the lipid bilayer with a histidine-purified actin-binding domain of fimbrin (FimA2) (Fig. 4*A*). At low FimA2 concentrations (R_{adh} = [fimA2]/[G-actin] = 10), the contraction is qualitatively similar to that observed with no adhesion but the length scale of contraction is reduced (Movie S14). As the adhesion to the membrane is increased (R_{adh} = 100–1,000), contraction is impeded further, evidenced by the formation of smaller aggregates that are spaced closer together (Fig. S6). Using sparse labeling of F-actin (1–2% fluorescent), we readily observe that the consequence of high adhesion is to dramatically constrain the transverse motions of F-actin and prevent buckling with large r_c (Fig. 4*B* and Movie S12). The r_c at which severing occurs is nearly identical to those observed in the absence of adhesion (Fig. 3*B*) but occurs with greater frequency due to adhesion constraints. As such, the rate of F-actin severing is dramatically enhanced in these networks (Fig. 4*C*). The resistance provided by membrane adhesion reduces filament translocation (Figs. S6 and S10 and Movies S12 and S14) and constrains bending to smaller radii of curvature, thereby impeding contraction but enhancing mechanically mediated severing.

Our data demonstrate a prominent role of F-actin bending and buckling in the contraction of nonsarcomeric actomyosin networks found in nonmuscle and smooth muscle cells. In striated muscle, contraction is facilitated by enhanced actomyosin

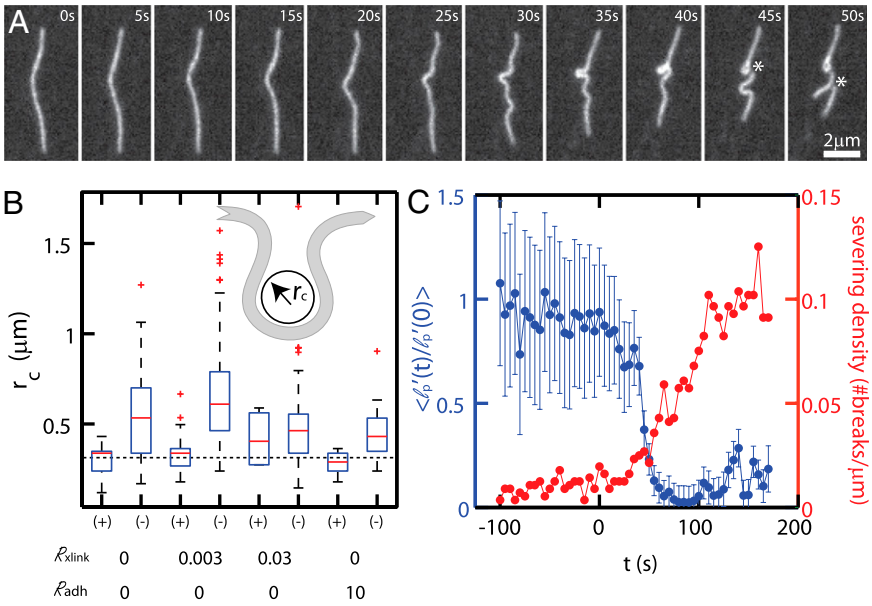

Fig. 3. Filament buckling at high curvature induces severing. (*A*) F-actin images during contraction of a sparsely labeled network (R_{xlink} = 0, R_{Adh} = 0). (*B*) Box plot of the filament radii of curvature r_c measured preceding a severing event (+) or not (–). Dashed line indicates 300 nm. The sample sizes for the different conditions are as follows: R_{xlink} = 0/R_{adh} = 0 (N_{sever} = 14, N_{stable} = 58), R_{xlink} = 0.003/R_{adh} = 0 (N_{sever} = 22, N_{stable} = 123), R_{xlink} = 0.03/R_{adh} = 0 (N_{sever} = 4, N_{stable} = 58), and R_{xlink} = 0/R_{Adh} = 10 (N_{sever} = 10, N_{stable} = 21). N_{sever} is the number of measurements of r_c taken that sever in the following time point. N_{stable} is the number of r_c measurements, selected at random, that do not sever in the next time point. Data reflect eight independent experiments. (*Inset*) Schematic of radius of curvature. (*C*) Persistence length normalized to initial value before contraction (blue) and mean severing density as a function of time (red) for R_{xlink} = 0.003/R_{Adh} = 0. The data reflect the curvature of 5 filaments (l_p') and the severing (N_{sever}) of 102 filaments from a single experiment.

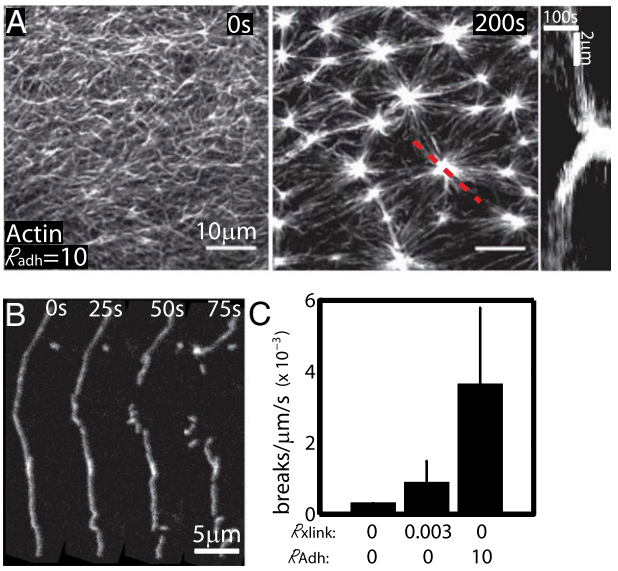

Fig. 4. Membrane adhesion modulates mechanically induced severing. (*A*) F-actin images in R_{Adh} = 10, R_{xlink} = 0. (*Left*) Precontraction, (*Middle*) postcontraction, and (*Right*) a kymograph of actin intensity for red dashed line. (*B*) Individual F-actin during contraction of a sparsely labeled network with R_{Adh} = 10, R_{xlink} = 0. (*C*) Severing rates for R_{xlink} = 0/R_{adh} = 0 (N_{fil} = 48, N_{expt} = 1), R_{xlink} = 0.003 (N_{fil} = 204, N_{expt} = 4), and R_{adh} = 10 (N_{fil} = 133, N_{expt} = 3). N_{fil} is the total number of filaments observed through a total of N_{exp} independent experiments.

overlap arising from tensile forces applied to F-actin with well-defined polarity (Fig. 5*A*). The extent of contraction is limited by the extent of increased overlap of myosin thick filaments and F-actin thin filaments and is ~30% for striated muscle (29). In actomyosin networks and bundles that lack such organization, myosin generates both compressive and tensile stresses on F-actin (Fig. 5*A*) (19). These stresses can arise either locally by the stochastic interactions of myosin motors directly on individual F-actin (15, 19) or from myosin-generated fluctuations of the surrounding network in which the filament is embedded (26). Filament portions under compressive stresses yield readily via buckling, thereby breaking the symmetry between compressive and tensile stresses that myosin motors generate in disordered actin networks. The remaining tensile stresses drive shortening of the filament segments to result in network contraction. Contraction persists over large strains as filament portions change from being under tension to compression as the network architecture dynamically changes during contraction. Thus, this contractility mechanism is robust to disorder and accommodates a large extent of contraction, as is observed in smooth and nonmuscle cells. Our data demonstrate that buckling can account for the contractile strains up to 60–80% at the initial stages of contraction; at later times, filament severing and reorganization may start to dominate further contraction and myosin-mediated remodeling but these later stages are not amenable to our analysis.

Here we demonstrate that local contractions can occur in quasi-2D networks containing myosin and actin alone. In these conditions, the length scale over which contraction occurs within the network is proportional to the F-actin length, consistent with poor network connectivity by myosin motors (30–33) or putative cross-linking by MC. Through the addition of the passive cross-linker α-actinin, we are able to increase the length scale of contraction to macroscopic length scales. Previous work in semidilute, 3D networks has shown the necessity of cross-linkers for contractility (30–33) whereas a sufficiently high density of myosin motors in the absence of cross-linkers is sufficient to facilitate contractility in 1D bundles (34). We attribute the differences in efficiency of myosin cross-linking observed under these diverse experimental conditions to changes in local concentration of actin and myosin. Our current findings appear to be consistent with a local concentration of actomyosin in a 2D network being between that of a semidilute 3D network and a highly dense 1D bundle.

Our results suggest that control of filament bending is an important regulator of contractility. In weakly cross-linked networks (R_{xlink} = 0–0.003), large radii of curvature are observed and facilitate a large extent of local network compression. As the cross-link concentration is increased and bundles are formed (R_{xlink} = 0.03), the filaments are constrained, thus reducing the mean radii of curvature and limiting the local compression. We speculate that filament bends and, thus, the regime of buckling-mediated contractility could be eliminated in the regime where myosin-generated stresses are reduced (e.g., by reduced myosin concentration or thick filament size) or have increased bundle bending rigidity. In this regime, other mechanisms of contractility arising from filament reorganization may occur (16).

We find that portions of F-actin that are bent to high curvature are prone to severing. This finding is consistent with previous measurements of mechanically mediated F-actin severing induced by externally applied or thermal forces (11, 35), which found that severing occurred at a radius of curvature of <0.4 μm (35) or an angle of 56° (11). In the absence of external mechanical constraints, such severing occurs with forces of 3–4 pN. By contrast, F-actin breakage under tension occurs at forces of ~400 pN (36). This discrepancy likely underlies the predominance of filament severing via buckling that we observe. Thus, F-actin severing enhances the asymmetric response to facilitate contractility of

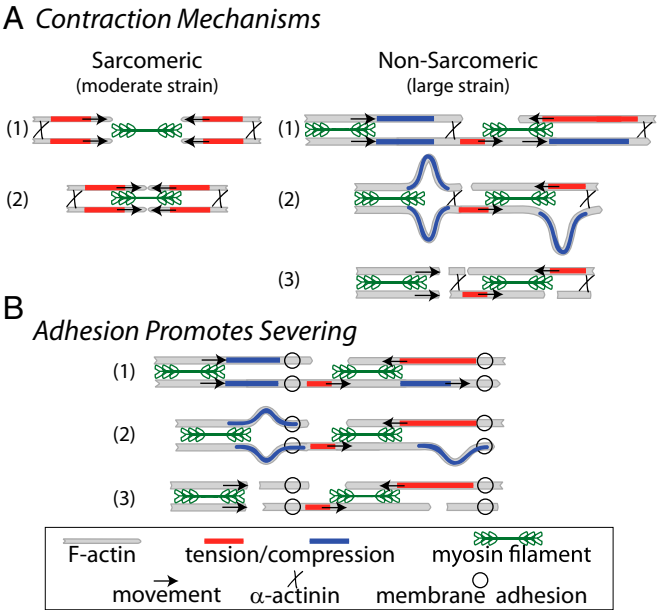

Fig. 5. Schematics of contraction mechanisms. (*A*) In sarcomeres, myosin filaments (green) are segregated toward pointed ends of F-actin and cross-links (black "x") are at the barbed end. This configuration permits solely tensile forces (red) and, thus, translocation of actin filaments (black arrows), resulting in contraction. In disordered, nonsarcomeric actomyosin bundles and networks that lack segregation of motors and cross-links, actomyosin interactions result in both tension and compression (blue). Compressive stresses are relieved through filament buckling and severing, keeping only tensile forces and, thus, driving contraction. (*B*) Cross-links to the membrane (open circles) spatially constrain stresses generated by motors and thus promote severing and prevent long-range transmission of tensile stresses. Numbers delineate sequential steps in each process.

disordered actomyosin. In addition to relieving compressive stress, severing creates F-actin barbed and pointed ends that change F-actin density and length. Whereas previous measurements have demonstrated a myosin-II–mediated destabilization of F-actin networks and bundles both in vitro (12, 37) and in vivo (4), our results demonstrate that these likely arise from compressive stresses generated within disordered networks. F-actin severing changes the local density of barbed and pointed filament ends, which, depending on the biochemical environment, can result in changes of polymer density. In the presence of capping protein or the absence of G-actin, F-actin would disassemble whereas, in the presence of formins or high concentrations of G-actin, actin polymerization would be stimulated (38). This demonstrates the importance of compressive stresses generated by actomyosin interactions in disordered networks as a mechanism to couple contractility and F-actin turnover, as has been reported in vivo (2–4). Such mechanically regulated F-actin polymerization dynamics may enhance or complement biochemical regulation by severing proteins such as ADF/cofilin.

In the presence of adhesion to the lipid bilayer, F-actins are subject to large compressive stresses that promote severing, but force transmission through the network is not permitted due to enhanced adhesive drag (Fig. 5*B*). Thus, adhesion of the cortical network to the membrane modulates the coordination between actomyosin contractility and filament severing, which may be a regulatory mechanism to coordinate cortex contractility and turnover in vivo. These results may explain the reduced contractility with enhanced cortical adhesion observed in vivo (39). Moreover, our results suggest that membrane adhesion could be a means to use actomyosin stresses to generate a high density of F-actin barbed ends, as is found at focal adhesion plaques in adherent cells (40). Contractility in our simplified, reconstituted system demonstrates the importance of the nonlinear mechanical response of individual actin filaments to compressive stresses, as their buckling is crucial for early symmetry breaking events to drive cortical actomyosin contractility and polymerization dynamics, which are necessary in cell physiology.

Methods

A supported lipid bilayer from egg phosphatidyl choline (91%) and nickel lipid (9%) is formed on a Piranha-treated coverslip glass surface. In conditions with membrane adhesion, a His-tagged actin-binding domain of fimbrin is added and allowed to bind to the membrane. In all experiments, 1.3 μM phalloidin-stabilized actin filaments (F-actin) are crowded to the lipid bilayer surface with a 0.25% methylcellulose solution for >15 min, after which α-actinin and myosin II are sequentially added and gently mixed. To prevent shear of the F-actin network proximal to the lipid bilayer, the α-actinin and myosin are mixed with a small-volume pipette in the immediate vicinity of the positioned objective. At elevated concentrations of α-actinin (R_{xlink} = 0.03) contraction is initiated through the inactivation of blebbistatin. All imaging is performed using spinning-disk confocal microscopy. Details of all experimental methods can be found in *SI Materials and Methods*.

ACKNOWLEDGMENTS. We thank Martin Lenz (Centre National de la Recherche Scientifique, Orsay, France) for his advice on calculations. We also thank Tobias Falzone and Yujie Li for providing purified proteins. M.L.G. acknowledges support from the Burroughs Wellcome Fund, the Packard Foundation, and National Institutes of Health Grant DP10D00354. This work was supported by the Materials Research Science and Engineering Center at University of Chicago. M.P.M. is funded by a postdoctoral fellowship from the National Science Foundation Institute for Complex Adaptive Matter (ICAM).

1. Bray D, White JG (1988) Cortical flow in animal cells. *Science* 239(4842):883–888.
2. Guha M, Zhou M, Wang YL (2005) Cortical actin turnover during cytokinesis requires myosin II. *Curr Biol* 15(8):732–736.
3. Medeiros NA, Burnette DT, Forscher P (2006) Myosin II functions in actin-bundle turnover in neuronal growth cones. *Nat Cell Biol* 8(3):215–226.
4. Wilson CA, et al. (2010) Myosin II contributes to cell-scale actin network treadmilling through network disassembly. *Nature* 465(7296):373–377.
5. Vicente-Manzanares M, Ma X, Adelstein RS, Horwitz AR (2009) Non-muscle myosin II takes centre stage in cell adhesion and migration. *Nat Rev Mol Cell Biol* 10(11):778–790.
6. Pollard TD (2010) Mechanics of cytokinesis in eukaryotes. *Curr Opin Cell Biol* 22(1):50–56.
7. Wozniak MA, Chen CS (2009) Mechanotransduction in development: A growing role for contractility. *Nat Rev Mol Cell Biol* 10(1):34–43.
8. Gardel ML, Schneider IC, Aratyn-Schaus Y, Waterman CM (2010) Mechanical integration of actin and adhesion dynamics in cell migration *Annu Rev Cell Dev Biol* 26:3.1–3.19.
9. Roh-Johnson M, et al. (2012) Triggering a cell shape change by exploiting preexisting actomyosin contractions. *Science* 335(6073):1232–1235.
10. Ponti A, Machacek M, Gupton SL, Waterman-Storer CM, Danuser G (2004) Two distinct actin networks drive the protrusion of migrating cells. *Science* 305(5691):1782–1786.
11. McCullough BR, et al. (2011) Cofilin-linked changes in actin filament flexibility promote severing. *Biophys J* 101(1):151–159.
12. Haviv L, Gillo D, Backouche F, Bernheim-Groswasser A (2008) A cytoskeletal demolition worker: Myosin II acts as an actin depolymerization agent. *J Mol Biol* 375(2):325–330.
13. Huxley HE (1969) The mechanism of muscular contraction. *Science* 164(3886):1356–1365.
14. Svitkina TM, Verkhovsky AB, McQuade KM, Borisy GG (1997) Analysis of the actin-myosin II system in fish epidermal keratocytes: Mechanism of cell body translocation. *J Cell Biol* 139(2):397–415.
15. Lenz M, Gardel ML, Dinner AR (2012) Requirements for contractility in disordered cytoskeletal bundles. *New J Phys* 14:033037.
16. Dasanayake NL, Michalski PJ, Carlsson AE (2011) General mechanism of actomyosin contractility. *Phys Rev Lett* 107(11):118101.
17. Kruse K, Joanny JF, Jülicher F, Prost J, Sekimoto K (2004) Asters, vortices, and rotating spirals in active gels of polar filaments. *Phys Rev Lett* 92(7):078101.
18. Vavylonis D, Wu JQ, Hao S, O'Shaughnessy B, Pollard TD (2008) Assembly mechanism of the contractile ring for cytokinesis by fission yeast. *Science* 319(5859):97–100.
19. Lenz M, Thoresen T, Gardel ML, Dinner AR (2012) Contractile units in disordered actomyosin bundles arise from f-actin buckling. *Phys Rev Lett* 108(23):238107.
20. Wang S, Wolynes PG (2012) Active contractility in actomyosin networks. *Proc Natl Acad Sci USA* 109(17):6446–6451.
21. Liverpool TB, Marchetti MC, Joanny JF, Prost J (2009) Mechanical response of active gels. *Europhys Lett* 85:18007.
22. Soares e Silva M, et al. (2011) Active multistage coarsening of actin networks driven by myosin motors. *Proc Natl Acad Sci USA* 108(23):9408–9413.
23. Köhler S, Lieleg O, Bausch AR (2008) Rheological characterization of the bundling transition in F-actin solutions induced by methylcellulose. *PLoS ONE* 3(7):e2736.
24. Courson DS, Rock RS (2010) Actin cross-link assembly and disassembly mechanics for alpha-Actinin and fascin. *J Biol Chem* 285(34):26350–26357.
25. Skau CT, et al. (2011) Actin filament bundling by fimbrin is important for endocytosis, cytokinesis, and polarization in fission yeast. *J Biol Chem* 286(30):26964–26977.
26. Brangwynne CP, Koenderink GH, Mackintosh FC, Weitz DA (2008) Nonequilibrium microtubule fluctuations in a model cytoskeleton. *Phys Rev Lett* 100(11):118104.
27. Howard J (2001) *Mechanics of Motor Proteins and the Cytoskeleton* (Sinauer, Sunderland, MA).
28. Saarikangas J, Zhao H, Lappalainen P (2010) Regulation of the actin cytoskeleton-plasma membrane interplay by phosphoinositides. *Physiol Rev* 90(1):259–289.
29. Gordon AM, Homsher E, Regnier M (2000) Regulation of contraction in striated muscle. *Physiol Rev* 80(2):853–924.
30. Janson LW, Kolega J, Taylor DL (1991) Modulation of contraction by gelation/solation in a reconstituted motile model. *J Cell Biol* 114(5):1005–1015.
31. Bendix PM, et al. (2008) A quantitative analysis of contractility in active cytoskeletal protein networks. *Biophys J* 94(8):3126–3136.
32. Köhler S, Schaller V, Bausch AR (2011) Structure formation in active networks. *Nat Mater* 10(6):462–468.
33. Backouche F, Haviv L, Groswasser D, Bernheim-Groswasser A (2006) Active gels: Dynamics of patterning and self-organization. *Phys Biol* 3(4):264–273.
34. Thoresen T, Lenz M, Gardel ML (2011) Reconstitution of contractile actomyosin bundles. *Biophys J* 100(11):2698–2705.
35. Arai Y, et al. (1999) Tying a molecular knot with optical tweezers. *Nature* 399(6735):446–448.
36. Tsuda Y, Yasutake H, Ishijima A, Yanagida T (1996) Torsional rigidity of single actin filaments and actin-actin bond breaking force under torsion measured directly by in vitro micromanipulation. *Proc Natl Acad Sci USA* 93(23):12937–12942.
37. Schmoller KM, Semmrich C, Bausch AR (2011) Slow down of actin depolymerization by cross-linking molecules. *J Struct Biol* 173(2):350–357.
38. Campellone KG, Welch MD (2010) A nucleator arms race: Cellular control of actin assembly. *Nat Rev Mol Cell Biol* 11(4):237–251.
39. Charras GT, Hu CK, Coughlin M, Mitchison TJ (2006) Reassembly of contractile actin cortex in cell blebs. *J Cell Biol* 175(3):477–490.
40. Gupton SL, Eisenmann K, Alberts AS, Waterman-Storer CM (2007) mDia2 regulates actin and focal adhesion dynamics and organization in the lamella for efficient epithelial cell migration. *J Cell Sci* 120(Pt 19):3475–3487.

Supporting Information

Murrell and Gardel 10.1073/pnas.1214753109

SI Materials and Methods

Buffers. G-buffer is composed of 2 mM Tris·HCl (pH 8.0) and 0.1 mM $CaCl_2$, 0.2 mM ATP, 1 mM Sodium Azide, and 0.5 mM DTT. F-buffer is composed of 10 mM Imidazole, 1 mM $MgCl_2$, 50 mM KCl, 0.2 mM EGTA, and 0.5 mM ATP (pH 7.5). The vesicle buffer is 100 mM NaCl, 20 mM Hepes (pH 7.3). The α-actinin buffer is 20 mM NaCl, 0.1 mM EDTA, 15 mM β-mercaptoethanol, and 20 mM Tris (pH 7.6). The storage buffer for the myosin is 0.5 mM Pipes (pH 7.0) and 0.45 M KCl.

Microscopy. A Nikon Ti inverted microscope with a 60× 1.4-Na oil immersion lens (Nikon) and equipped with a spinning-disk confocal (CSUX; Yokagawa) was used. The model cortex is imaged at 491 nm, 568 nm, and 647 nm every 5 s for 15 min on a CCD camera (Coolsnap HQ2; Photmetrics) controlled by Metamorph (MDS Analytical Technologies). Photobleaching experiments were performed with a 405-nm laser by a micromirror array that controls local excitation (Mosaic; Photonics Instruments) with a 2-s exposure and a circular region of 20 μm in diameter.

Sample Chamber. A custom-built sample chamber (Chamlide) consists of two aluminum plates with 17-mm circular holes drilled in their center that sandwich a 25-mm round coverslip and a rubber gasket with an inner diameter of 1.7 cm and thickness of 0.5 cm. This creates an open, circular sample well amenable to high-resolution imaging with dimensions similar to that of the gasket that can hold ∼1 mL of fluid volume to enable sequential addition of proteins. To prevent evaporation over long times, a 40 × 50-mm coverslip is overlaid on the top surface of the open chamber.

Preparation of Reconstituted Cortex. Egg phosphatidyl choline (EPC, 91%; Avanti Polar Lipids), nickel lipid [1,2-di-(9Z-octadecenoyl)-sn-glycero-3-([N-(5-amino-1-carboxypentyl)iminodiacetic acid]succinyl) (DGS-NTA), 8.8%; Avanti Polar Lipids], and FITC Green 1,2-Dihexadecanoyl-sn-Glycero-3-Phosphoethanolamine (DHPE) (Molecular Probes; 0.2%) are combined and dried in a glass container under N_2 gas. For simplicity, throughout the text, we do not mention the DHPE when reporting membrane composition as it is used only as a fluorescent reporter. We therefore name only two compositions: 91% EPC/9% NTA and 100% EPC (or "pure EPC"). These compositions are then resuspended by vortexing in vesicle buffer and sonicated in a bath sonicator for upward of 10 min. The resultant small, unilamellar vesicles (SUVs) are added to a 25-mm Piranha-treated coverslip in a custom-built imaging chamber (Chamlide) (∼2 mL) for 5 min to fuse and form a fluid bilayer. The membrane is washed and kept hydrated in ∼500 μL F-buffer (minus ATP). To bind the actin to the membrane specifically, a truncated, recombinant fimbrin that contains a single actin-binding site, FimA2 [pET-21a-MBP-FimA1A2p-His, gift of Dave Kovar, University of Chicago, Chicago (1)] in ATP-free F-buffer, is added before addition of the F-actin and incubated for 15 min. This His-FimA2 is localized to the surface, using a specific interaction between the nickel lipid and the His-tag on the FimA2 (Fig. S1 *A*, *B*, *H*, and *I*). The membrane is subsequently washed with ATP-free F-buffer (immediately before addition of actin) with a final volume of ∼500 μL.

Stable actin filaments are formed by polymerizing 2.0 μM dark G-actin [prepared from chicken breast, gift of Yujie Li (University of Chicago, Chicago) and Dave Kovar] and 0.64 μM Alexa-568 G-actin (Cytoskeleton) mixture in F-buffer supplemented with 0.5% methylcellulose [molecular weight (MW), 14,000], 4.0 μM dark phalloidin (Cytoskeleton), and 9% glucose oxidase/catalase (Calbiochem) for 2 h on ice. A total of 500 μL of F-actin is added to the membrane (containing 500 μL ATP-free F-buffer), such that the final concentration of F-actin is 1.32 μM and the ATP concentration is 250 nM. The F-actin is allowed to sediment to the surface of the bilayer for a minimum of 15 min such that the accumulation of F-actin approaches a plateau (Fig. S1 *C*–*G* and Movie S1). To cross-link the F-actin, a highly concentrated solution of α-actinin (Sigma) is added after the F-actin is crowded to the surface. The α-actinin is allowed to bind the network also for a minimum of 15 min, a time longer than required to associate and bundle the actin network (Fig. S3*E*). Rabbit skeletal muscle myosin (Cytoskeleton) that has been labeled with Alexa Fluor 647 in myosin storage buffer is then added to a final concentration of 50 nM. As the myosin storage buffer is at 0.45 M KCl, myosin is added as dimers, but assembles thick filaments within minutes when immersed into F-buffer.

The sample chamber volume (1 mL) increases by less than 2% total by the addition of both α-actinin and myosin as they are added in high concentrations. Both α-actinin and myosin are added slowly and in a circular fashion with a 20-μL pipette tip to the top of the sample volume, directly above the positioned objective. The sample is mixed by exchanging volumes and slow motions with this same, small pipette tip within ∼5 mm around the objective to not disturb the actin near the bilayer-coated coverslip. As the sample volume is large compared with the mixing volume, this method of mixing prevents disturbance of the F-actin and lipid bilayer. As the α-actinin and myosin dimer are small and diffuse quickly, this method yields homogenous protein concentrations within the actin sheet over length scales much larger than our imaging area (60×, ∼150-μm diameter viewing area).

Induction of Contraction. In un-cross–linked actin networks (R_{xlink} = 0), and networks with low concentrations of crosslinker (R_{xlink} = 0.003), contraction occurs rapidly and heterogeneously throughout the sample after the formation of thick filaments of myosin (Figs. S6 and S8). As the length scale of contraction is small, we can easily visualize the contractile domain and calculate a network strain via methods described below and in Fig. S5. In highly cross-linked (R_{xlink} = 0.03) samples, however, the length scale of contraction is too large to effectively calculate a strain (Movie S8). We therefore desire to spatially localize the contraction of the network to within the field of view. Before the addition of myosin, we add 40 μM blebbistatin, which allows for the polymerization and binding of myosin, but inhibits its ATPase activity (Fig. S8 *C*–*F*). We then inactivate blebbistatin through the local illumination of the sample with 491 nm light (2), thereby inducing myosin ATPase activity and contraction. Subsequently, we image the F-actin (568 nm) and myosin (647 nm). This process then repeats for all frames in the time course. Spatially controlling the contractility of a highly cross-linked network allows us to assess the buckling and severing of F-actin in a highly cross-linked sample with high accuracy (Fig. S8 *C*–*F*). Furthermore, we do this on 100% EPC bilayer to remove all traces of adhesion.

Calculation of F-actin Network and Single F-actin Strain. The x, y, t coordinates of myosin thick filaments were identified by their peak fluorescence in Imaris (Bitplane; Fig. S5*A*). Individual pairs of thick filaments were chosen opposite the radial zone of contraction. They are separated by an initial distance, w_0. Over time, this distance will decrease to measure $w(t)$ and the strain is therefore calculated as $\varepsilon_{network}(t) = 1 - w(t)/w_o$ (Fig. S5 *B*–*D*).

Similarly, the end-to-end filament length, L_0, was measured by hand with ImageJ for each point in time, t. The strain is then calculated from the fractional change in the end-to-end filament length compared with the initial length, $\varepsilon_{\text{filament}}(t) = 1 - L(t)/L_o$.

Calculation of Actomyosin Density in Contractile Zone. A circular region was drawn around the foci that are generated by contraction via Metamorph. The integrated fluorescent actin and myosin intensity that falls within that region is measured as a function of time (ImageJ).

Calculation of Persistence Length. The tangent correlation (C(s)) is calculated by taking the mean cosine of the angles ($\theta(s)$) between two segments along an arc length, s. First, the coordinates of the filament are obtained using the ImageJ plugin JFilament. Then, custom-written MATLAB routines are used to calculate C(s) and to fit an "effective" persistence length, ℓ'_p, as

$$\langle C(s)\rangle = \langle \cos(\vartheta(s) - 0)\rangle = e^{\frac{-s}{2\ell p}}. \quad \textbf{[S1]}$$

$\ell'_p(t)$ is calculated for all time points t before and after the formation of myosin thick filaments (Fig. S9).

Determination of Myosin Thick Filament Size, Shape, and Dynamics. Myosin thick filaments are identified as puncta by their local relative intensities and characterized as surface objects, using Imaris (Bitplane). A myosin puncta is an individual object if its fluorescence intensity is significantly higher than background. From the fluorescence intensity, the number of myosin thick filaments (myosin density), average thick filament velocity, thick filament shape (oblate ellipticity), and mean intensities can be calculated as a function of time during contraction (Fig. S4 *A* and *B*). When overlaid with the strain of the network, the thick filaments finish elongating (minimum in the oblate ellipticity) and then begin to contract (rise in the network strain). During contraction the oblate ellipticity increases again, as thick filaments become round aggregates of myosin. We take the correspondence between the onset of network strain and a minimum in thick filament elongation to mean that myosin adsorption to the F-actin network is minimal past this stage, although we cannot rule out the possibility of minor adsorption of myosin dimers.

The lengths of myosin thick filaments were determined by drawing linescans over deconvolved fluorescence images (Fig. S4*C*). The linescans are drawn by hand and yield a profile of intensity over space (Fig. S4*D*). The half-maximum (half-max) width of the linescan is used to determine the width of the myosin thick filaments (Fig. S4*E*). This yields an average myosin thick filament length of 1.5 μm ± 0.3 μm and constitutes ∼400 heads per thick filament (3). As a single myosin head has a duty ratio of ∼2% under low load, approximately four crossbridges make contact between thick and thin filaments at any given time. If we assume that each motor head contributes force additively, and each motor head can exert 3–4 pN force (4), then the thick filament can exert roughly 12–16 pN of force at low load. As myosin affinity is load dependent, the maximal force exerted could increase under tension up to ∼600 pN.

Determination of F-Actin Radius of Curvature. The radii of curvature in Fig. 3 are calculated by drawing circular regions along buckling F-actin in ImageJ. From the measured area of the circular regions, the radii are calculated. Only filaments that would have <2 μm radius of curvature are selected. The radius of curvature in Fig. S10*E* is calculated by taking the inverse of the curvature, $(\mathrm{d}\theta/\mathrm{ds})^{-1}$ of the individual skeletonized F-actin over time.

Calculation of the F-Actin Severing Rate. The severing rate was calculated by identifying individual filaments through segmentation routines in Imaris (Bitplane). Segmented F-actins are discriminated on the basis of their fluorescence intensity over a background intensity and their separation distance from each other (Fig. S10*A*). Over time, as filaments sever, there are more segmented objects detected. Subtracting the number of filaments at $t = 0$ (before the formation of myosin thick filaments) from the number of filaments for all subsequent times, t, yields the number of breakage events (as a function of t) due to myosin activity. Normalizing the total number of breakage events by the total length of all filaments before severing yields the number of breaks per micrometer over time. We show that breakage of filaments is due to myosin activity, as the number of filaments remains constant before the addition of myosin (Fig. S10*B* and Movie S13) but increases after myosin thick filament assembly ($t > 0$, Fig. S10*C* and Movie S10). The fluctuation in the severing rate before the thick filaments of myosin is due to the error in identifying individual filaments that occurs, for example, when two filaments overlap and are counted as one by the segmentation algorithm.

Severing is attributed to compression if in the image immediately before the severing event (5 s earlier), the F-actin has a radius of curvature below ∼5 μm (Fig. S10 *D* and *E*). For straight filaments with immeasurably high radius of curvature, severing is attributed to tension (Fig. S10*F*). The latter is uncommon, and we estimate the upper limit on severing due to tension compared with all severing events is ∼0.2% for ($R_{\text{xlink}} = 0$, $R_{\text{adh}} = 0$) and ∼1% for ($R_{\text{xlink}} = 0$, $R_{\text{adh}} = 10$). We discriminate tensile events by visual inspection, counting the number of filaments by hand that appear to fit the aforementioned criteria.

Assessment of F-Actin Bundling. Methylcellulose (MC) (0.2%) is known to induce minor bundling of 3D solutions of elevated concentrations of F-actin (5). Therefore, we wanted to ensure that our 2D, dilute solutions of F-actin (1 μM) are filamentous and not significantly bundled in the presence of 0.25% MC. To do so, we quantitatively assessed the extent of bundling in our non-cross–linked network at 0.25% MC ($R_{\text{xlink}} = 0$) and compared this to the bundling observed in a non-cross–linked network ($R_{\text{xlink}} = 0$) at an elevated MC level (0.44%) and a highly cross-linked network ($R_{\text{xlink}} = 0.03$) (Fig. S3 *A*–*F*). First, we take linescans of the fluorescent F-actin over a region of ∼20 μm. Then, we calculate the average intensity (μ) and SD of the fluorescence intensity (σ) of the F-actin. We then call the quotient, σ/μ, the bundling parameter to assess the amount of bundling that occurs during the sedimentation of an F-actin network at 0.25%, the bundling of the network that occurs as MC is elevated from 0.25% to 0.44%, and the bundling of the network as R_{xlink} is increased from 0 to 0.03 (Fig. S3*G*). From this calculation, we can see that there is a minimal increase in the bundling parameter as F-actin is sedimented to the surface of a phospholipid bilayer (Fig. S3*G*, green line). Although the mean F-actin fluorescence intensity increases due to the accumulation of F-actin, its SD does not increase significantly (Fig. S3*B*). However, bundling is evident both visually (Fig. S3 *C* and *E*) and quantitatively (Fig. S3 *D* and *F*) with both elevated concentrations of MC or α-actinin. The bundling that occurs during the elevation of the MC concentration is both due to the effect of bundling of already sedimented F-actin (Fig. S3*C*, 270 s) and due to the further sedimentation of additional F-actin that remained in solution (Fig. S3*C*, 570 s). This increase in the bundling of F-actin is also similar to the effect of elevated concentrations of α-actinin (Fig. S3*G*).

Thus, we estimate that bundling of our non-cross–linked F-actin network in the presence of 0.25% MC is minimal, although we cannot exclude that MC likely has some effect on F-actin/F-actin interactions or promotes small regions of clustered filaments.

Assessment of F-Actin Alignment. Upon the sedimentation of F-actin by 0.25% methylcellulose, filaments have a random local orientation, but align in time as F-actin accumulates (Movie S2). To reduce the alignment of actin, before F-actin addition, we incubate the 91% EPC/9% NTA bilayer in 0.2% BSA for 15 min

before washing it out. Subsequently, the addition of F-actin results in a network with less alignment (Movie S3, 1–2% filaments labeled) than if not treated with BSA. The contraction of this less-aligned F-actin network results in length scales qualitatively similar to those of the contraction of unaligned filaments (20.5 ± 3.3 μm for BSA-treated membrane and 20.0 ± 8.8 μm for untreated membrane, Movie S6).

Effects of MC on Contraction. To confirm that our experimental conditions were not sensitive to MC concentration, we repeated measurements with 0.15% MC, the minimum concentration required to crowd F-actin to the bilayer surface (Fig. S2), and found qualitatively similar contractility to that in experiments with 0.25% MC (Fig. S7).

SI Text and Equations

The sliding of entangled F-actin well coupled to a fluid bilayer is subject to high drag, both through the viscosity of the membrane and through the viscosity of the surrounding actin solution. We estimate our membrane viscosity is ~1.4 Pa*s, ~500 times the viscosity of the surrounding medium. To pull a 15-μm filament through this viscosity at roughly 150 nm/s (the strain rate of entangled networks) would generate a drag of ~5.2 pN, which is much greater than the force required to buckle it (~3 nN). This can account for the enhanced severing of a membrane-bound actin network. Furthermore, this is again a lower estimate of the viscosity, as it excludes the contribution from the surrounding filament entanglements that are effectively enhanced by the adhesion itself.

Calculation of Membrane Viscosity. To calculate the diffusivity from the fluorescence recovery after photobleaching (FRAP) data, we use Eq. **S2**, where w is the radius of the bleached spot, and $t_{1/2}$ is the time it takes to recover half of its integrated intensity (6):

$$D = \frac{w^2}{4t_{1/2}}. \qquad \textbf{[S2]}$$

The measured diffusivity of FITC-DHPE in a primarily EPC bilayer is $D = 3.8 \times 10^{-12}$ m^2/s, which is in good agreement with that of Texas Red DHPE in EPC membranes on glass of 1.7×10^{-12} m^2/s (7) and Pure EggPC bilayers (4.0×10^{-12}) (8).

FRAP on RFP-His yields a diffusivity of 6.5×10^{-13} m^2/s. To calculate the membrane viscosity η_m, from the RFP-His [using the radius, r of a GFP barrel of 1.2 nm (9)], we use the Saffman–Delbruck formalism for Stokes Einstein:

$$D(r) = \frac{k_B T}{4\pi\eta_m}\left[\ln\left(\frac{\eta_m}{\eta_w}\frac{1}{r}\right) - \gamma + \frac{1}{2}\right]. \qquad \textbf{[S3]}$$

This yields a 2D membrane viscosity η_m, of 4.5×10^{-9} Ns/m. The 3D membrane viscosity is

$$\eta_{3D} = \frac{\eta_m}{h}. \qquad \textbf{[S4]}$$

For a bilayer thickness, $h = 3.3$ nm, we get a 3D membrane viscosity of 1.36 Pa*s. The typical ranges for 3D membrane viscosities are in the range of 3–151 Pa*s (10). This is considerably higher than the viscosity of 0.25% methylcellulose (MW, 14,000) in water (~2 mPa*s; Sigma).

Calculation of Drag Force. Using the following equations, we calculate the drag on an individual filament bound to the phospholipid bilayer,

$$D = \mu k_B T \qquad \textbf{[S5]}$$

$$\mu = \frac{v}{F}, \qquad \textbf{[S6]}$$

where μ is the viscous mobility of an individual nickel lipid and D is the diffusivity of the nickel lipid as determined by the FRAP of His-RFP bound to it. This yields a force, $F = 9.5 \times 10^{-16}$ N to move a single nickel lipid at 150 nm/s (the rate of contraction). We consider this to be the contribution by an individual lipid molecule to the drag. For an actin filament 15 μm in length, there should be a total of 5,454 monomers. As there is an excess of FimA2 to actin, we approximate that every monomer of actin is bound to the surface, and the total force would then be 5.2 pN. This assumes each lipid contributes independently, which is an approximation, as there should be asymmetry in the direction of the applied force. This does not include the resistance due to the F-actin network itself.

Calculation of the Buckling Force. F-actin that is compressed at ends that are free to rotate but not move laterally will buckle under the force given by Eq. **S7**. For a bending stiffness of $k = 7.3 \times 10^{-26}$ N/m^2 (11), and a filament length $L = 0.94$ μm, the corresponding force and energy to buckle are

$$f_b = \frac{\pi^2 k}{L^2} = 0.82 \text{ pN} \qquad \textbf{[S7]}$$

$$E_b = \frac{kL}{2r_c^2} = 3.8 \times 10^{-19} \text{ J}, \qquad \textbf{[S8]}$$

where r_c is the radius of curvature equal to 300 nm. As a single skeletal muscle dimer can exert ~3–4 pN of force (4), it can easy buckle an actin filament at the preferred radius of curvature of 300 nm. This corresponds to the measured 0.9 pN and 1.2×10^{-18} J to bend a single actin filament into a knot with a 0.18-μm radius (12). As we measure contraction for filament lengths longer than 1 μm, buckling is possible for all realizable filament lengths within this assay.

The force to rupture a filament under tension is as high as 500 pN (13). Taking this over the spacing between actin monomers of 5.3 nm corresponds to an association energy of 2.65×10^{-18} J. Therefore, the energetic cost of bending a single F-actin to 300 nm is less than the cost of rupturing. This is consistent with the nondeterministic severing of F-actin at this radius of curvature, but with its enhanced probability (12).

1. Skau CT, Kovar DR (2010) Fimbrin and tropomyosin competition regulates endocytosis and cytokinesis kinetics in fission yeast. *Curr Biol* 20(16):1415–1422.
2. Sakamoto T, Limouze J, Combs CA, Straight AF, Sellers JR (2005) Blebbistatin, a myosin II inhibitor, is photoinactivated by blue light. *Biochemistry* 44(2):584–588.
3. Morimoto K, Harrington WF (1974) Substructure of the thick filament of vertebrate striated muscle. *J Mol Biol* 83(1):83–97.
4. Finer JT, Simmons RM, Spudich JA (1994) Single myosin molecule mechanics: Piconewton forces and nanometre steps. *Nature* 368(6467):113–119.
5. Köhler S, Lieleg O, Bausch AR (2008) Rheological characterization of the bundling transition in F-actin solutions induced by methylcellulose. *PLoS ONE* 3(7):e2736.
6. Axelrod D, Koppel DE, Schlessinger J, Elson E, Webb WW (1976) Mobility measurement by analysis of fluorescence photobleaching recovery kinetics. *Biophys J* 16(9):1055–1069.
7. Hovis JSB, Boxer SG (2001) Patterning and composition arrays of supported lipid bilayers by microcontact printing. *Langmuir* 17:3400–3405.
8. Albertorio F, et al. (2005) Fluid and air-stable lipopolymer membranes for biosensor applications. *Langmuir* 21(16):7476–7482.
9. Hink MA, et al. (2000) Structural dynamics of green fluorescent protein alone and fused with a single chain Fv protein. *J Biol Chem* 275(23):17556–17560.
10. Cicuta P, Keller SL, Veatch SL (2007) Diffusion of liquid domains in lipid bilayer membranes. *J Phys Chem B* 111(13):3328–3331.

11. Gittes F, Mickey B, Nettleton J, Howard J (1993) Flexural rigidity of microtubules and actin filaments measured from thermal fluctuations in shape. *J Cell Biol* 120(4):923–934.
12. Arai Y, et al. (1999) Tying a molecular knot with optical tweezers. *Nature* 399(6735): 446–448.
13. Tsuda Y, Yasutake H, Ishijima A, Yanagida T (1996) Torsional rigidity of single actin filaments and actin-actin bond breaking force under torsion measured directly by in vitro micromanipulation. *Proc Natl Acad Sci USA* 93(23):12937–12942.

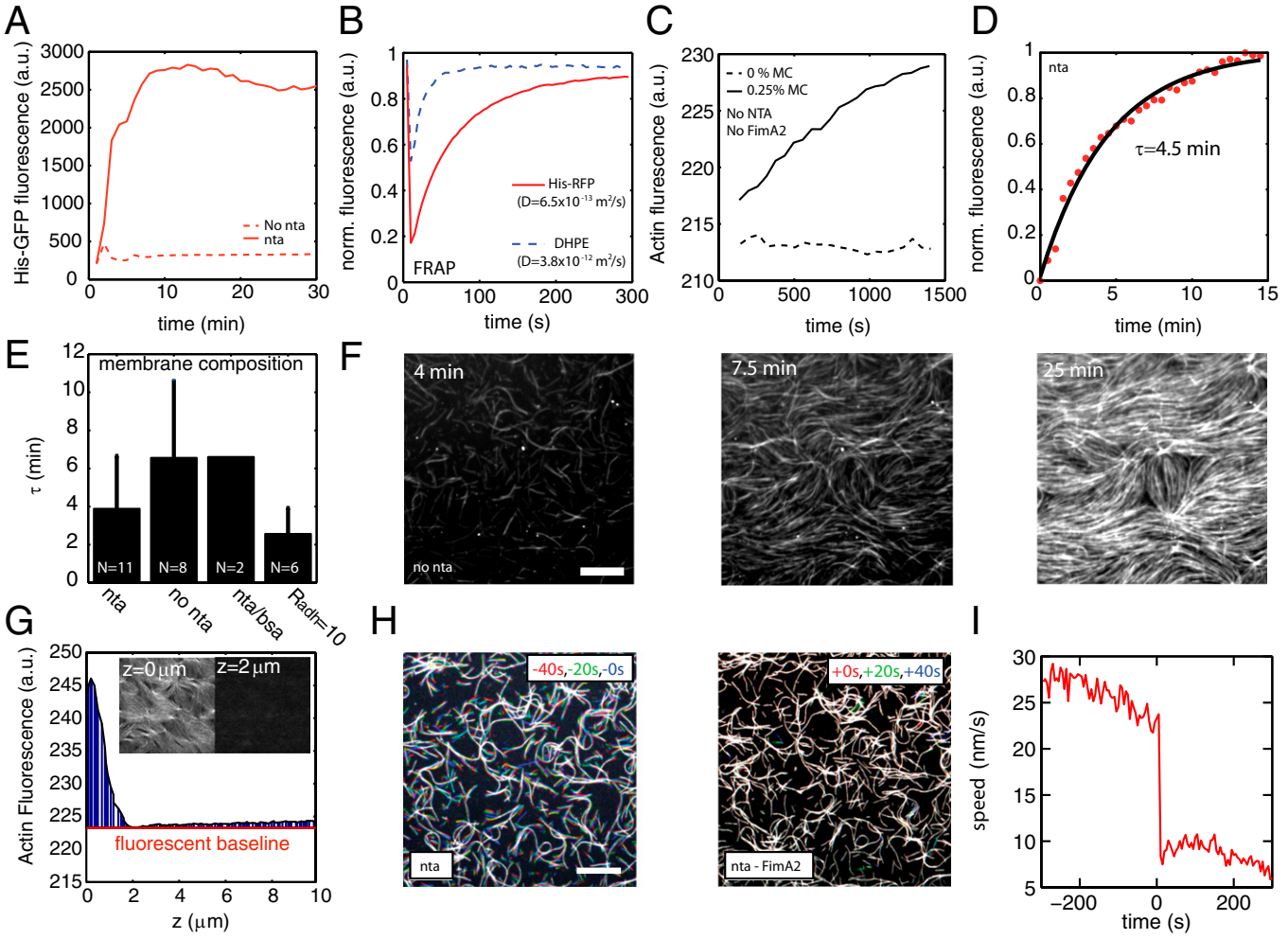

Fig. S1. Localizing proteins to the model membrane by specific and nonspecific interactions. (*A*) His-tagged green fluorescent protein (His-GFP) intensity at the surface of the supported lipid bilayer as a function of time for 91% EPC/9% NTA membranes (NTA, solid line) vs. 100% EPC membranes (No NTA, dashed line). His-GFP is added at 0 s. (*B*) Fluorescence recovery after photobleaching (FRAP) experiment of FITC-DHPE (blue line) and His-tagged red fluorescent protein (His-RFP) to measure the mobility of DHPE and NTA lipids, respectively. Bleaching of intensity occurs shortly after 0 s and complete recovery is observed within 300 s. The diffusion coefficient of each species is indicated. (*C*) Accumulation of F-actin at the surface of a pure EPC phospholipid bilayer by measurement of the intensity of fluorescent actin over time. The addition of 0.25% methylcellulose (MC) crowds F-actin to the surface of the membrane (solid line) but without MC it does not associate to the membrane (dotted line). There is no FimA2 or any other molecule to specifically bind the F-actin present on the bilayer. (*D*) Normalized mean fluorescence intensity of actin over time (red dots) during accumulation on an EPC/NTA membrane after addition of F-actin at 0 min. The rise time that reflects the dynamics of F-actin accumulation (black line) is fitted with $y = b_1 - b_2 * e^{(-t/tc)}$. (*E*) The rise time, t_c, for different compositions of membrane: 91% EPC/ 9% NTA (NTA), 100% EPC (no NTA), and 91% EPC/9% NTA with 15-min 0.2% BSA wash step (NTA/bsa) and with specific adhesion via incubation of 91%EPC/9%NTA membrane with 10 μM His-FimA2 (R_{Adh} = 10). (*F*) Fluorescence micrographs 4, 7.5, and 25 min after the crowding of F-actin to the surface of a 100% EPC bilayer (no NTA), using 0.25% MC. (Scale bar, 10 μm.) (*G*) Mean F-actin fluorescence intensity vs. distance from the phospholipid bilayer (*z*) as acquired from a confocal *z*-stack of an F-actin network crowded to the surface of a bilayer with 0.25% MC. (*Insets*) Fluorescent micrographs of the F-actin network adjacent to the bilayer (z = 0 μm) and 2 μm above the bilayer (z = 2 μm). (*H*, *Left*) An overlay of F-actin (1–2% labeled) at three successive time points (20-s intervals, in red, blue, and green) before the addition of FimA2 shows high filament mobility. (*H*, *Right*) An overlay of three successive time points after addition of FimA2 show drastically reduced filament mobility. Before F-actin sedimentation, the EPC/NTA bilayer is incubated in 0.2% BSA for 15 min. (Scale bar, 10 μm.) (*I*) Instantaneous velocity of short (2 μm) filaments from *H*. Before the addition of His-FimA2 (t < 0), these filaments are highly mobile, but are significantly less mobile after the addition of His-FimA2 at t = 0 s.

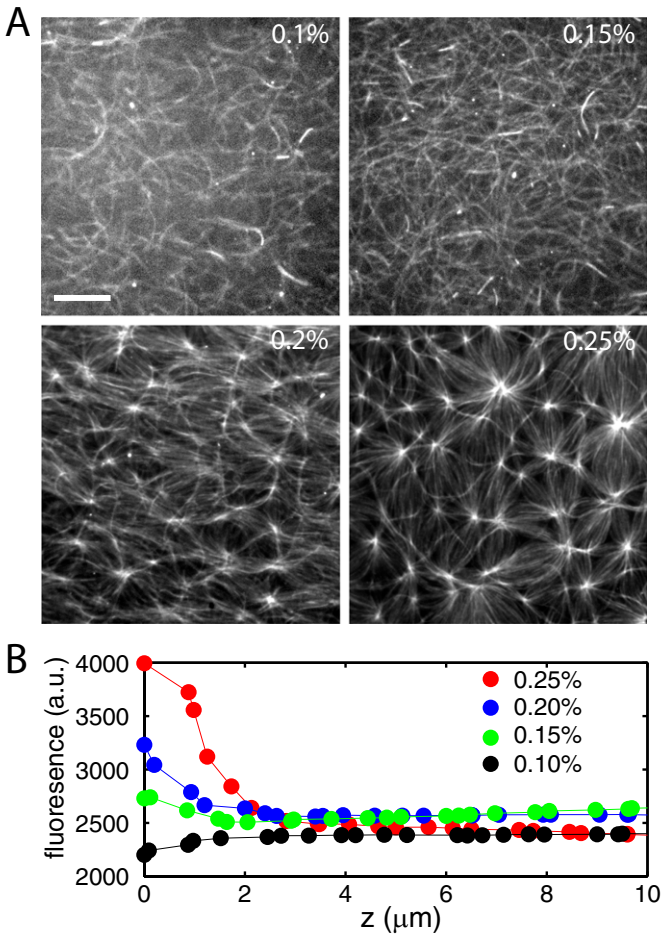

Fig. S2. Effects of MC on F-actin crowding. (*A*) F-actin sedimented to the surface of a phospholipid bilayer (pure EPC) under varying concentrations of methylcellulose (0.1%, 0.15%, 0.2%, and 0.25%). (Scale bar, 10 μm.) Images were taken on a spinning-disk confocal microscope. (*B*) Mean F-actin fluorescence intensity away from the bilayer surface (*z*) for varying methylcellulose concentrations. Below a 0.15% methylcellulose concentration, F-actin does not accumulate on the bilayer surface.

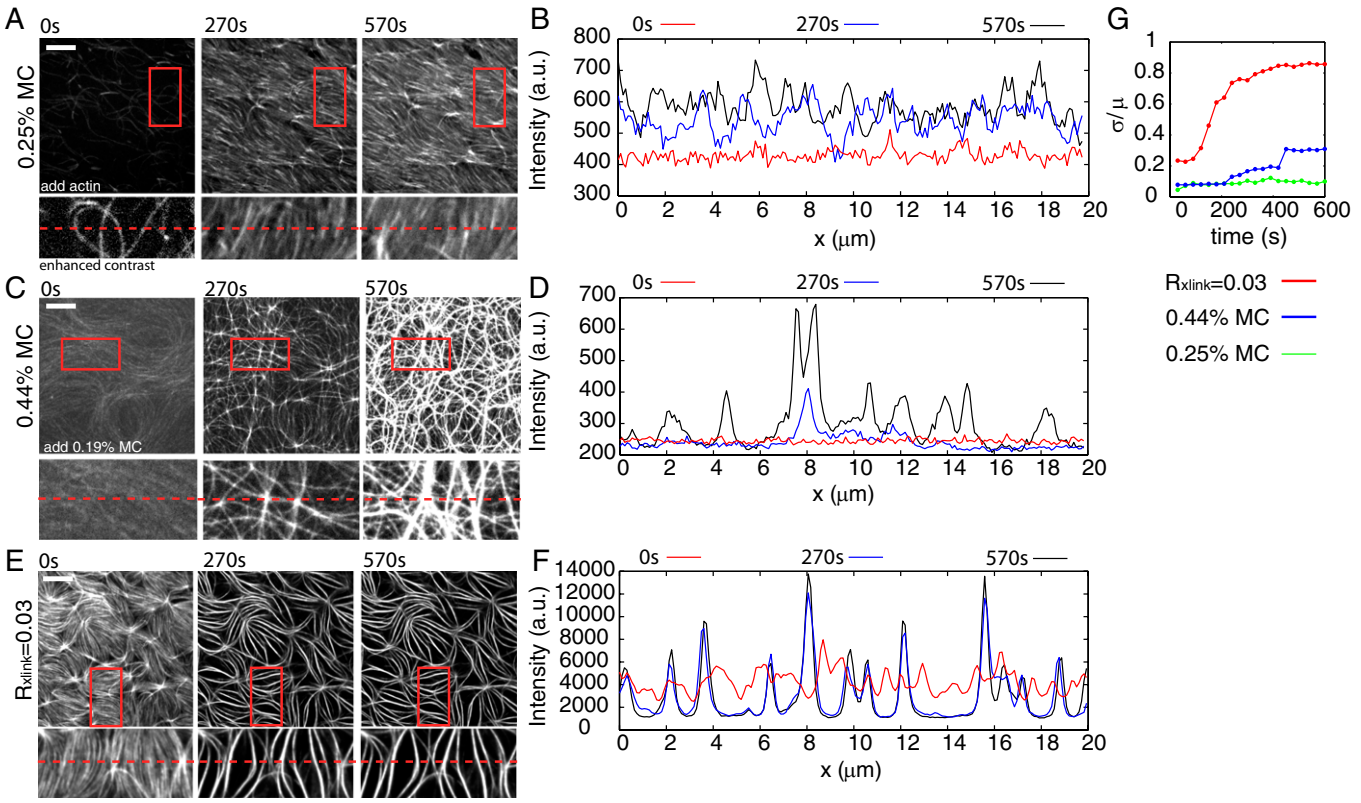

Fig. S3. Effects of MC and α-actinin on forming F-actin bundles. (*A*) (*Upper*) Fluorescence micrographs 0 s, 270 s, and 570 s after the crowding of F-actin to the surface of a phospholipid bilayer (91% EPC/9% NTA), using 0.25% methylcellulose (MC) after addition of 1 μM fluorescent F-actin at $t = 0$ s. Red rectangle indicates region that is zoomed in and shown in the *Lower* part. Dotted red line indicates zone used for linescan in *B*. (*C*) Zero seconds, 360 s, and 750 s after the increase of MC from 0.25% to 0.44% of an existing F-actin layer. At $t = 0$, the F-actin layer at 0.25% methylcellulose is already present, and additional MC is added to yield a total MC concentration of 0.44%. Dotted red line indicates zone used for linescan in *D*. (*E*) Zero seconds, 420 s, and 570 s after the addition of α-actinin (1:30 actin:α-actinin) to an F-actin layer. At $t = 0$, α-actinin is added to an F-actin network at 0.25% MC to yield $R_{xlink} = 0.03$. Dotted red line indicates zone used for linescan in *F*. (Scale bars: 10 μm.) (*G*) Calculation of the SD (σ) divided by the mean (μ) in fluorescence over the linescans in *B*, *D*, and *F*.

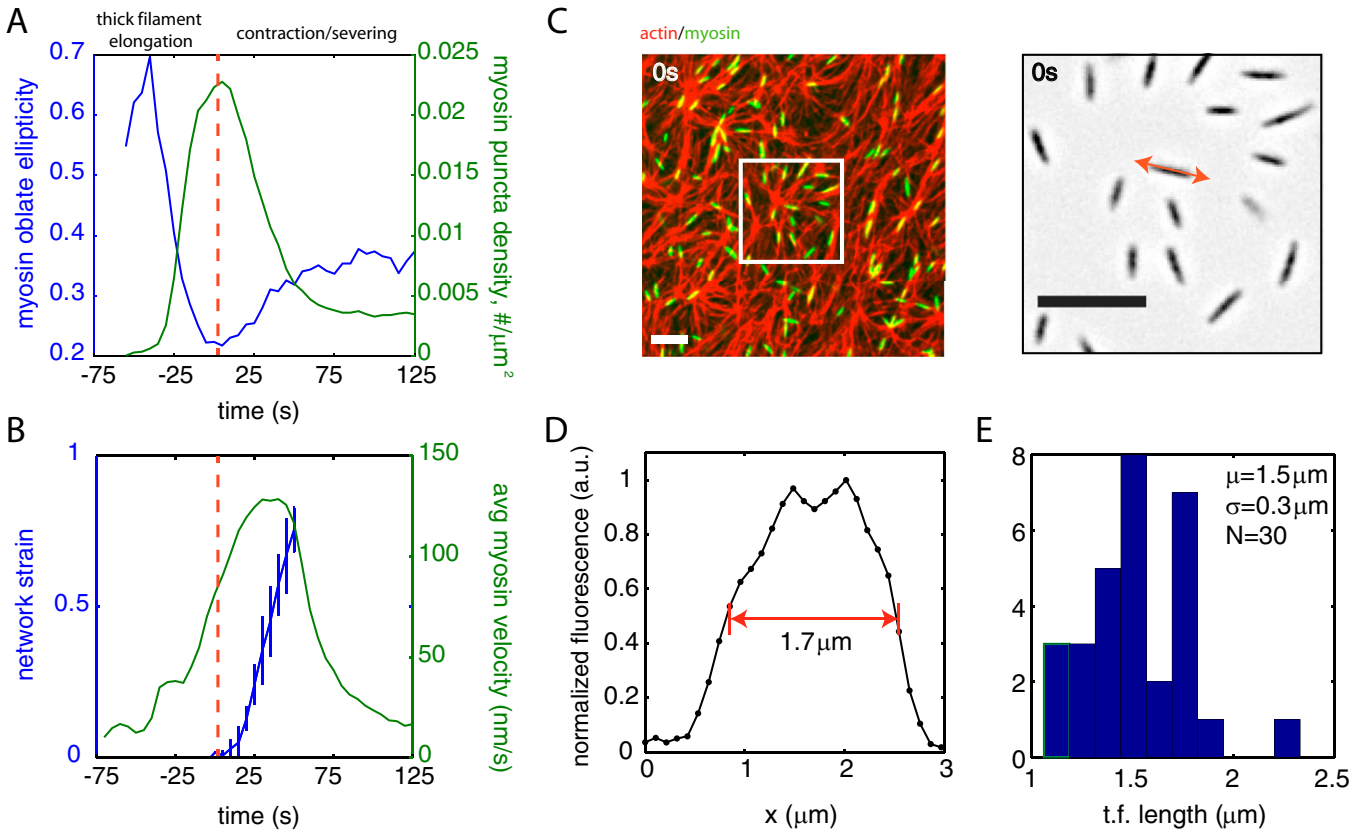

Fig. S4. Myosin thick filaments elongate before contraction. (*A*) Myosin shape (oblate ellipticity, blue) and myosin density (no. puncta/μm^2, green) measured over the time course of contraction. The red dotted line indicates the point where the elongation of the myosin thick filaments ends (minimum in the myosin oblate ellipticity). Oblate ellipticity increases during aggregation processes. (*B*) Network strain (blue) and myosin speed (green) over time. The red line has the same time as in *A*. Thus, time over which thick filament elongation and accumulation occur is before that of contraction. (*C*) F-actin network (red) and myosin thick filaments (green) at $t = 0$ s. (Scale bar, 5 μm.) White box indicates zoomed-in region shown to the *Right*. The contrast is inverted, and the red line indicates the location of a fluorescent linescan (of the original contrast) of the myosin thick filament. (Scale bar, 5 μm.) (*D*) Linescan of the myosin thick filament indicated in *C*. Red line indicates roughly the half-max width of the thick filament fluorescence. (*E*) Histogram of 30 different thick filament widths showing mean length of 1.5 μm.

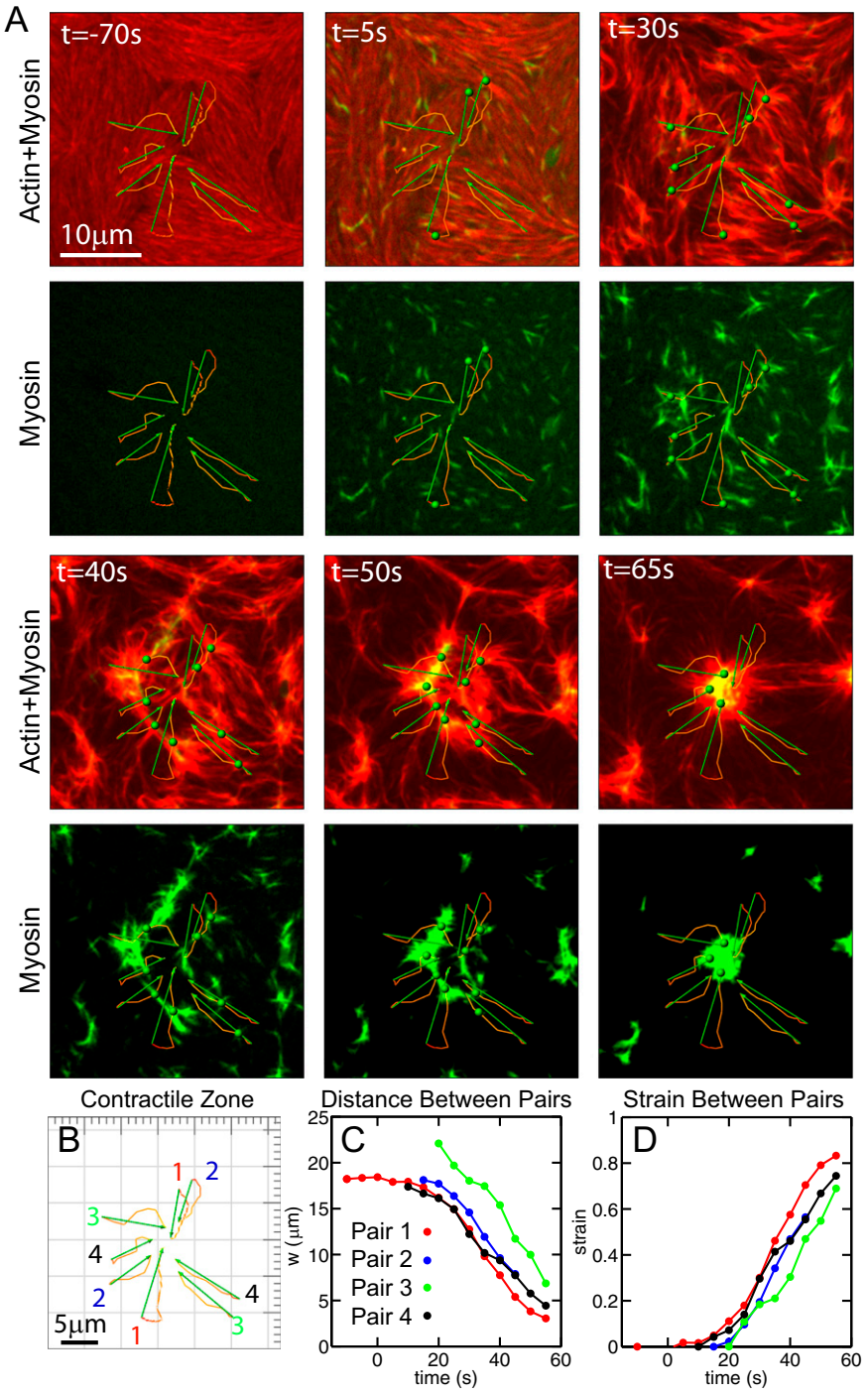

Fig. S5. Calculation of network strain by myosin tracking. (*A*) Time course of the contraction of the network shown in Fig. 1. (*Top*) Actin (red) and myosin (green) are combined and overlaid; (*Bottom*) myosin alone (green). The initial appearances of thick filaments of myosin are identified by a spot-tracking algorithm, which follows their movement over time (Imaris; Bitplane). In each section, the net displacement vectors (green arrows) and full displacement trajectories (red/orange lines) are plotted. As thick filaments of myosin appear, they are marked and followed over time, indicated in each color-combined image as a green dot. (*B*) Pairs of myosin thick filaments that are moving toward each other (and that later merge into aggregates) are chosen to measure the network strain. (*C*) The distance between the myosin pairs *w* decreases over time. (*D*) Contractile strain calculated from data in *C* over time. As shown in Fig. 1, these results are consistent with the kymography measurement.

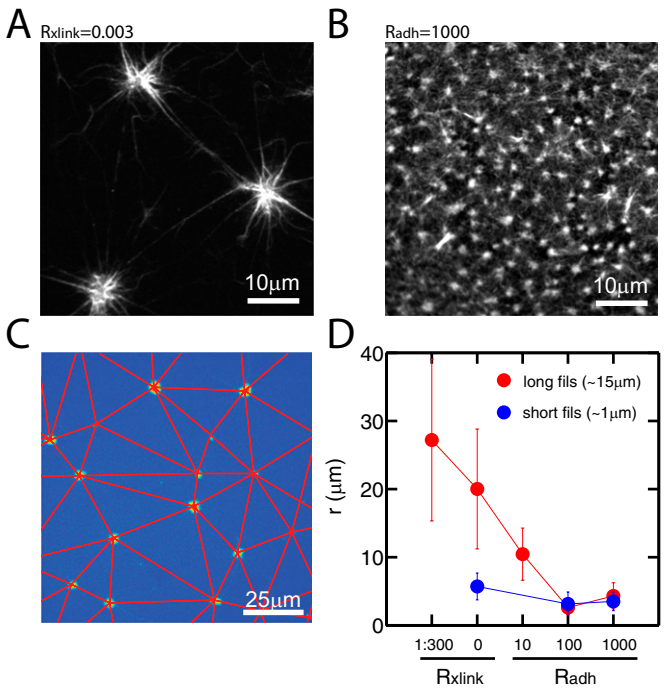

Fig. S6. Filament length, cross-linker, and filament–bilayer adhesion modulate the length scale of contraction. (*A*) Fluorescent actin images of R_{xlink} = 0.003, R_{adh} = 0 sample after contraction. (*B*) Fluorescent actin images of R_{adh} = 1,000 (R_{xlink} = 0) after contraction. (*C*) Image of myosin intensity (pseudocolor) after contraction is completed, with high-intensity regions corresponding to contracted "foci". The distance between contracted foci that appear after contraction has completed is measured by Voronoi tessellation, which identifies the distance to nearest neighbors for every focus (removing double-counted sides). The distance between these foci provides a measure of the size of the contractile domain *r*. (*D*) Bar plot of the length scale *r* of contraction ("contractile domain") as a function of concentration of cross-linker via α-actinin (R_{xlink}) and adhesion via His-FimA2 (R_{adh}). N_{length} dictates the number of measurements for separation length between foci, and N_{exp} is the number of independent experiments. For long (~15 μm) F-actin (red symbols), the sample sizes for the different conditions are as follows: R_{xlink} = 0 (N_{length} = 957, N_{exp} = 4), 0.003 (N_{length} = 755, N_{exp} = 3), and adhesion R_{adh} = 10 (N_{length} = 13,736, N_{exp} = 6), 100 (N_{length} = 18,372, N_{exp} = 1), and 1,000 (N_{length} = 3,402, N_{exp} = 1). For short F-actin (~1 μm sheared ~30 times with a Hamilton syringe, blue symbols), the associated sample sizes are R_{adh} = 0 (N_{length} = 677, N_{exp} = 1), R_{adh} = 100 (N_{length} = 45,309, N_{exp} = 2), and R_{adh} = 1,000 (N_{length} = 5,150, N_{exp} = 1).

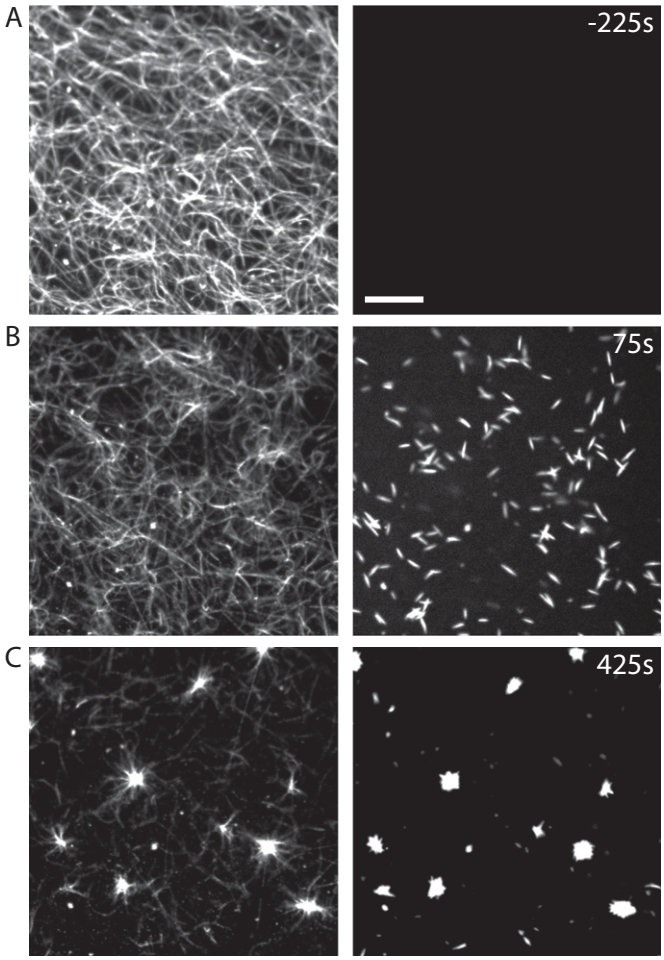

Fig. S7. MC concentration does not qualitatively alter contraction. (*Left*) Images of F-actin (1.32 μM) labeled with Alexa 568 crowded to the surface of a pure EPC bilayer with 0.15% MC. (*Right*) Skeletal muscle myosin II (16.7 nM) labeled with Alexa 647 at (*A*) $t = -225$ s, (*B*) 75 s, and (*C*) 425 s. Myosin thick filaments are fully assembled at $t = 0$ s and contraction is qualitatively consistent with results of Fig. 1, performed at 0.25% MC. (Scale bar, 10 μm.)

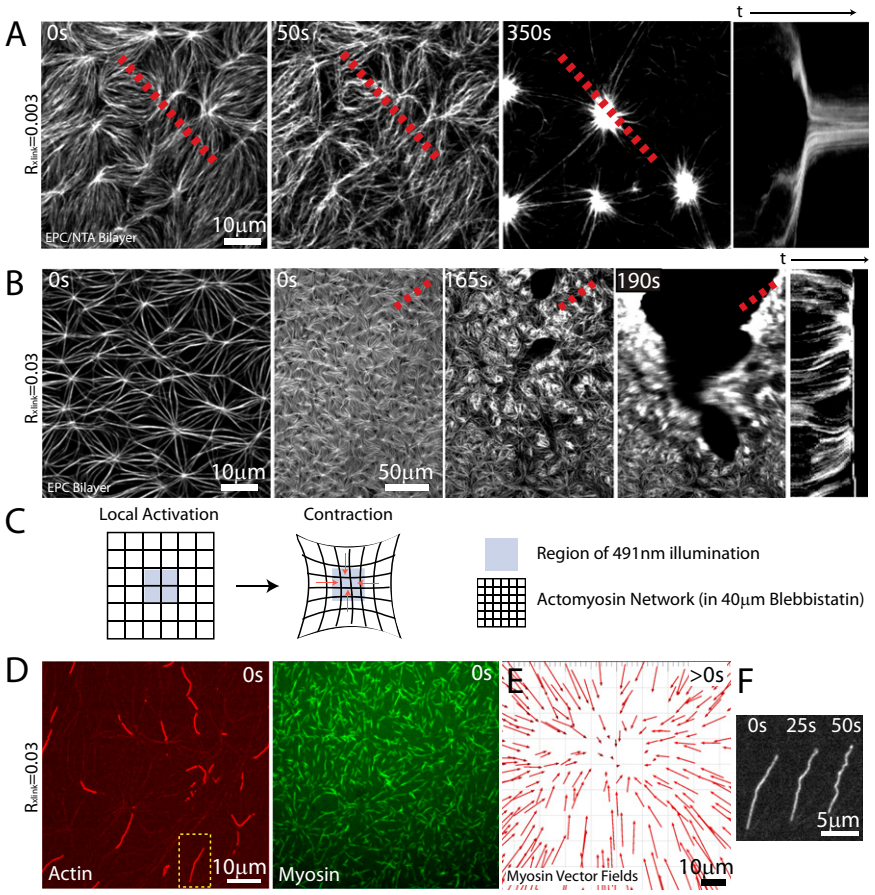

Fig. S8. Contraction of cross-linked networks and local induction of contraction by blebbistatin inactivation. (*A*) Fluorescent actin images on 91%EPC/9%NTA membrane cross-linked with low α-actinin (R_{xlink} = 0.003) with myosin addition at t = 0 s. (*Right*) Kymograph of red dashed line. (*B*) (*Left*) Fluorescent actin images on 100% EPC membrane bundled with high concentrations of α-actinin (R_{xlink} = 0.03). (*Right*) Zoomed-out region of R_{xlink} = 0.03 showing ripping and movement of entire domain. Myosin filaments appear at t = 0 s. (*C*) Diagram of the selective activation of myosin II activity to spatially and temporally control the contraction of the F-actin network. The black square grid represents the F-actin network decorated with myosin II whose ATPase activity is globally inhibited by 40 μM blebbistatin. The blue square within represents the region of the network that is selectively illuminated with 491 nm light, which inactivates blebbistatin, thereby inducing contraction. The red arrows indicate the inward movement of the F-actin network during contraction. (*D*) A sparsely labeled F-actin network (R_{xlink} = 0.03) (*Left*) and myosin II thick filaments (*Right*) before illumination with 491 nm light. The yellow dotted region is highlighted in *F*. (*E*) The inward contraction of the F-actin network can be visualized by the displacement of myosin II thick filaments, shown in Movie S9. (Scale bar, 10 μm.) (*F*) The local induction of contraction of a sparsely labeled F-actin network results in the buckling of F-actin within bundles at short wavelength. The illumination of the sample by 491 nm light, and thus myosin activation, occurs at 0 s.

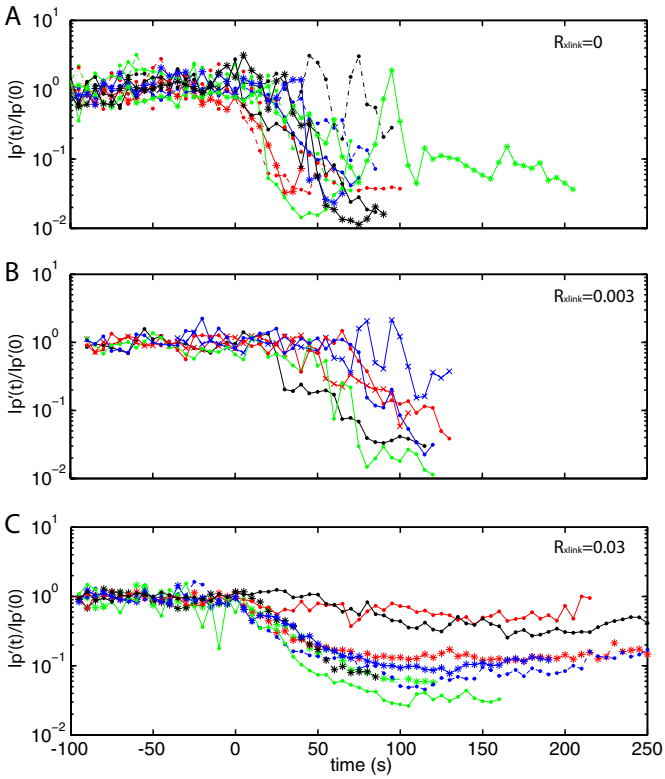

Fig. S9. Tangent correlation for multiple filaments. (*A–C*) Normalized tangent correlation, $l_p'(t)/l_p'(0)$ shown for multiple filaments for (*A*) R_{xlink} = 0 (n = 12 filaments), (*B*) R_{xlink} = 0.003 (n = 6 filaments), and (*C*) R_{xlink} = 0.03 (n = 6 filaments). The normalization constant, $l_p'(0)$, is the tangent correlation before myosin thick filament formation, which occurs at t = 0.

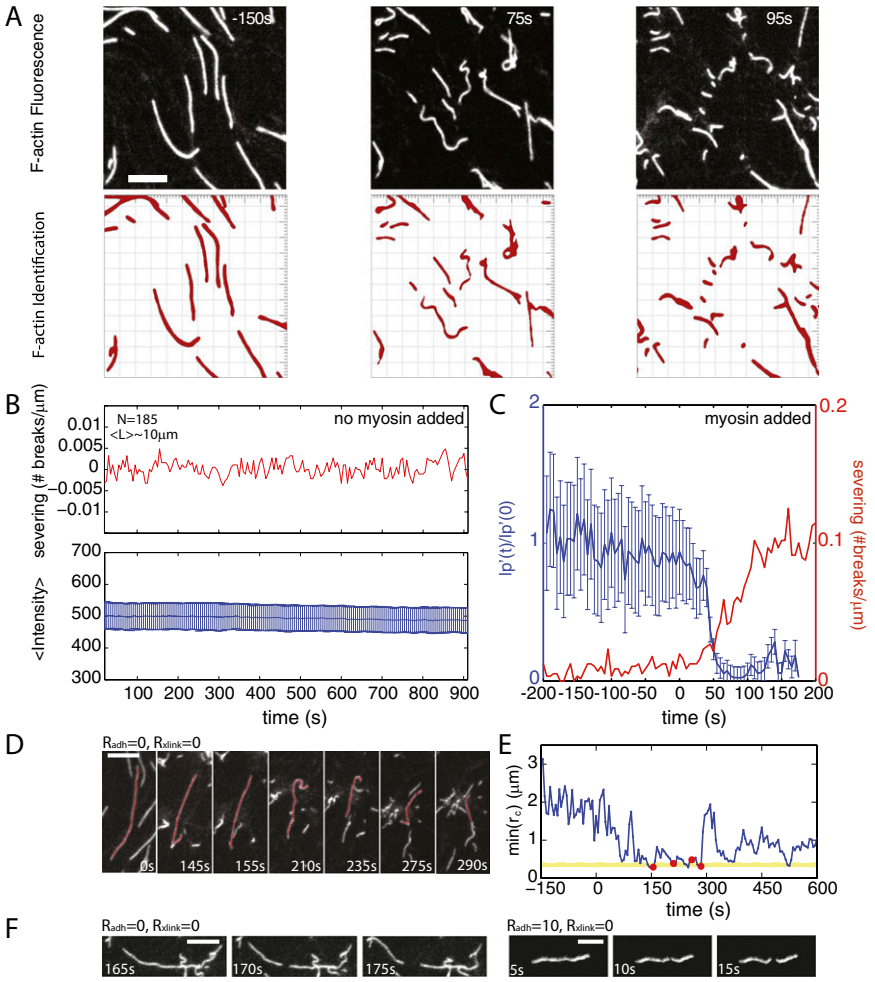

Fig. S10. Severing of F-actin during contraction. (*A*) (*Upper*) Fluorescent actin images in a sparsely labeled F-actin network (1–2%) (R_{xlink} = 0, R_{adh} = 0). The formation of thick filaments of myosin II occurs at t = 0 s. (*Lower*) Filament identification and segmentation are used to count the number of filaments in a sample region. The number of filaments changes with time as myosin contracts the F-actin network. The difference in the number of identified filaments at any time t and the number of filaments for t = 0 constitutes the number of severing events. (Scale bar, 5 μm.) (*B*) Severing rate (*Upper*) and average fluorescent actin intensity over time (*Lower*) of an actin network before the addition of myosin, showing no severing or significant change in intensity. The F-actin network is imaged every 5 s for 910 s and data are shown in Movie S13. (*C*) Severing rate (red) and normalized effective persistence length (blue) before and after the formation of myosin thick filaments at t = 0. Severing depends on myosin II activity, as severing increases only after t = 0. (*D*) Sparsely labeled F-actin network (R_{adh} = 0, R_{xlink} = 0), highlighting a single F-actin (red line) as it undergoes multiple severing events. (Scale bar, 5 μm.) (*E*) The minimal radius of curvature for the outlined filament in *D*. The red dots indicate the time points where a severing event has occurred. The yellow line indicates the region of r_c = 300–400 nm. (*F*) (*Left*) Sparsely labeled F-actin network with no (R_{adh} = 0, R_{xlink} = 0) and moderate adhesion (R_{adh} = 10, R_{xlink} = 0) that shows the apparent breakage due to tension. We estimate that 1% of severing events are due to tension for R_{adh} = 0, R_{xlink} = 0 and 5% of severing events are due to tension for R_{adh} = 10, R_{xlink} = 0. (Scale bar, 5 μm.)

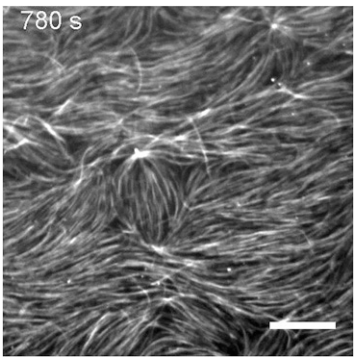

Movie S1. Methylcellulose-induced crowding of F-actin to a bilayer surface. Shown are images of F-actin labeled with Alexa 568 (red) crowded to the surface of a 91% EPC/9% NTA supported bilayer over time. At 0 s, 1.32 μM F-actin is added to buffer containing 0.25% methylcellulose. (Scale bar, 10 μm.)

Movie S1

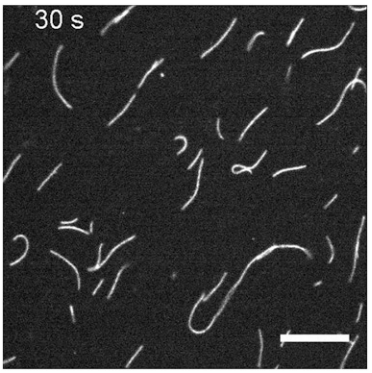

Movie S2. F-actin sedimentation aligns filaments. Shown are images of F-actin labeled with Alexa 568 (0.03 μM) in a network of dark F-actin (1.0 μM), crowded to the surface of a 91% EPC/9% NTA bilayer. One to 2% of the total actin filaments are labeled. At 0 s, F-actin is added to buffer containing 0.25% methylcellulose. (Scale bar, 10 μm.)

Movie S2

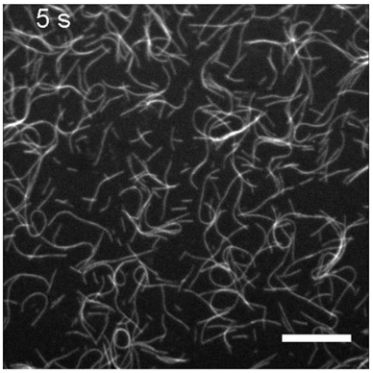

Movie S3. F-actin sedimentation onto BSA-treated bilayer reduces filament alignment. Shown are images of F-actin labeled with Alexa 568 (0.03 μM) in a network of dark F-actin (1.0 μM), crowded to the surface of a 91% EPC/9% NTA phospholipid bilayer that has been incubated in 0.2% BSA for 15 min and subsequently washed. One to 2% of the total actin filaments are labeled. At 0 s, F-actin is added to buffer containing 0.25% methylcellulose. (Scale bar, 10 μm.)

Movie S3

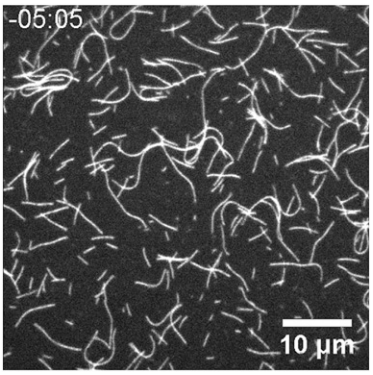

Movie S4. His-FimA2 immobilizes F-actin on the 91% EPC/9% NTA bilayer (R_{Adh} = 1,000). Low concentration (~0.1 μM) of F-actin is crowded to the surface by 0.25% MC of a 91% EPC/9% NTA bilayer treated with 0.2% BSA (and subsequently washed). At 00:00, 1 mM His-FimA2 is added to bind individual F-actin to NTA lipid bilayers and, thus, immobilizing them. Time is in min:s.

Movie S4

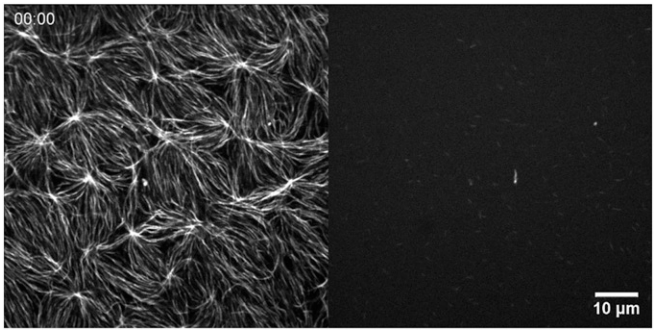

Movie S5. Contraction of un-cross–linked network (R_{xlink} = 0, R_{Adh} = 0). (*Left*) Images of F-actin (~1.32 μM) labeled with Alexa 568 crowded to the surface of 91% EPC/9% NTA bilayer. (*Right*) Skeletal muscle myosin II (50 nM) labeled with Alexa 647 is added to the network and assembles at t = 0 s. Time is in min:s.

Movie S5

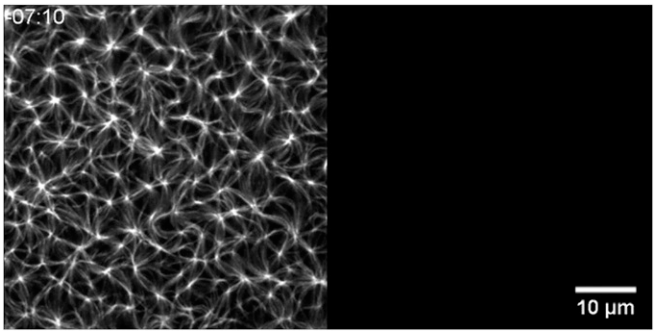

Movie S6. Contraction of an F-actin network with reduced alignment (R_{xlink} = 0, R_{Adh} = 0). (*Left*) Images of F-actin (~1.32 μM) labeled with Alexa 568 crowded to the surface of a 91% EPC/9% NTA bilayer that has been incubated in 0.2% BSA for 15 min and subsequently washed, thereby altering filament organization. (*Right*) Skeletal muscle myosin II (50 nM) labeled with Alexa 647 is added to the network and polymerizes at t = 0 s. Time is in min:s.

Movie S6

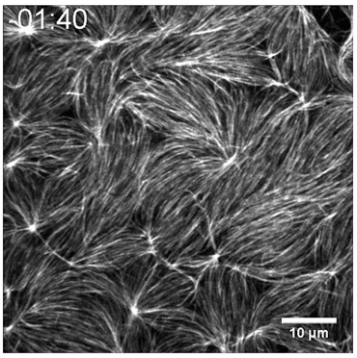

Movie S7. Contraction of isotropically cross-linked networks (R_{xlink} = 0.003, R_{Adh} = 0). Shown are images of F-actin (~1.32 μM) labeled with Alexa 568 crowded to the surface of a 91% EPC/9% NTA bilayer, cross-linked with low α-actinin (3 nM, R_{xlink} = 0.003), and then contracted with 50 nM skeletal muscle myosin filaments (not shown for clarity) added at 00:00. Time is in min:s.

Movie S7

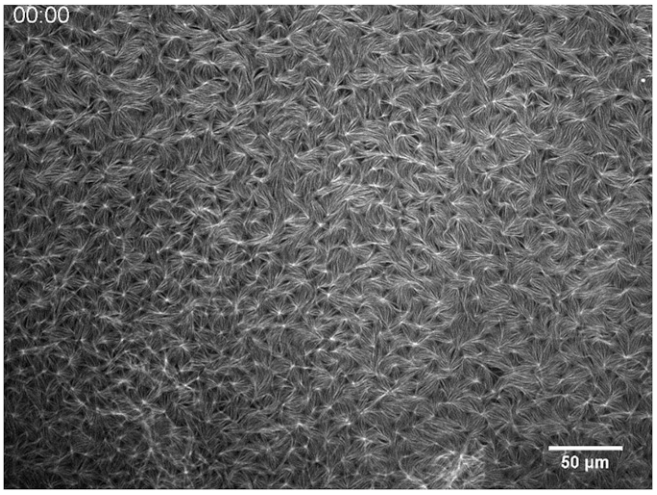

Movie S8. Contraction of bundled networks (R_{xlink} = 0.03, R_{Adh} = 0). Shown are images of F-actin (~1.32 μM) labeled with Alexa 568 crowded to the surface of a 100% EPC bilayer and cross-linked and bundled with high concentrations of α-actinin (30 nM, R_{xlink} = 0.03) and then contracted with 50 nM skeletal muscle myosin (not shown for clarity) at 00:00. Time is in min:s.

Movie S8

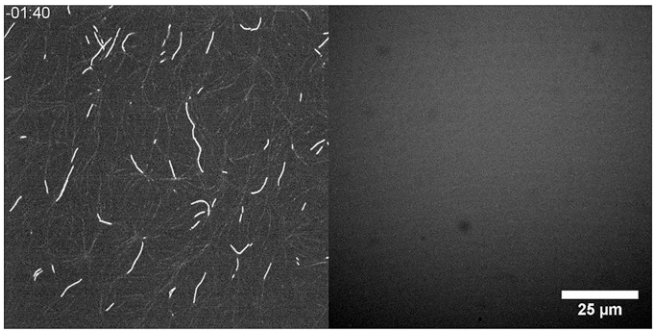

Movie S9. Local contraction of bundled network via blebbistatin (sparsely labeled filaments, R_{xlink} = 0.03, R_{Adh} = 0). (*Left*) Images of F-actin labeled with Alexa 568 (0.03 μM) in a network of dark F-actin (1.0 μM), crowded to the surface of a 100% EPC bilayer and cross-linked with 30 nM α-actinin (R_{xlink} = 0.03). Blebbistatin (40 μM) was present during the polymerization of the actin. (*Right*) Thick filaments of 50 nM myosin assemble at 00:00, and upon imaging the region with 491 nm light, the blebbistatin is inactivated and permits local myosin ATPase activity to drive contraction (Fig. S8).

Movie S9

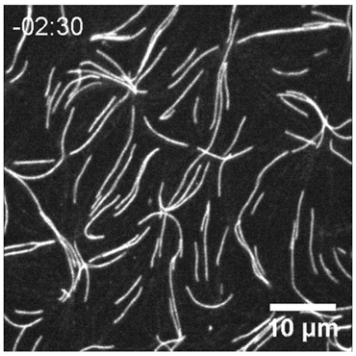

Movie S10. Contraction of un-cross–linked network (sparsely labeled filaments, $R_{xlink} = 0$, $R_{Adh} = 0$). Shown are images of F-actin labeled with Alexa 568 (0.03 μM) in a network of dark F-actin (1.0 μM) and crowded to the surface of a 91% EPC/9% NTA bilayer. The F-actin network is contracted with 50 nM skeletal muscle myosin (not seen), which assembles at 00:00. Time is indicated in min:s.

Movie S10

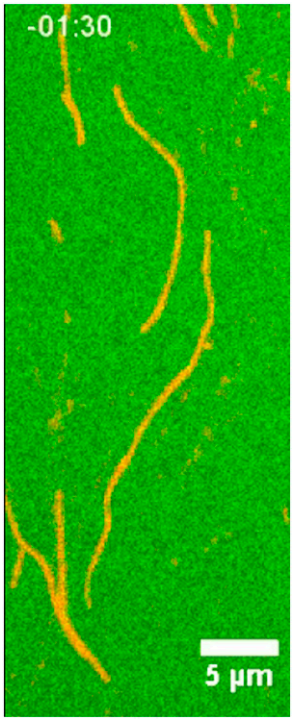

Movie S11. Myosin walking at different rates induces buckling (sparsely labeled filaments, $R_{xlink} = 0.003$, $R_{Adh} = 0$). Shown are images of F-actin (~1.32 μM) labeled with Alexa 568 (red) crowded to the surface of a 91% EPC/9% NTA bilayer, cross-linked with low α-actinin (3 nM, $R_{xlink} = 0.003$), and then contracted with 50 nM skeletal muscle myosin filaments (green), which assemble at 00:00 (Fig. 2*B*).

Movie S11

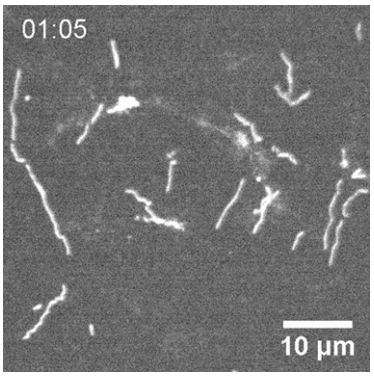

Movie S12. Contraction of adherent network (sparsely labeled filaments, R_{xlink} = 0, R_{Adh} = 10). Shown are images of F-actin labeled with Alexa 568 (0.03 μM) in a network of dark F-actin (1.0 μM) crowded to the surface of a 91% EPC/9% NTA bilayer incubated with 10 μM of His-FimA2 (R_{Adh} = 10). Skeletal muscle myosin II filaments (50 nM) (not shown for clarity) assemble at 00:00. Time is in min:s.

Movie S12

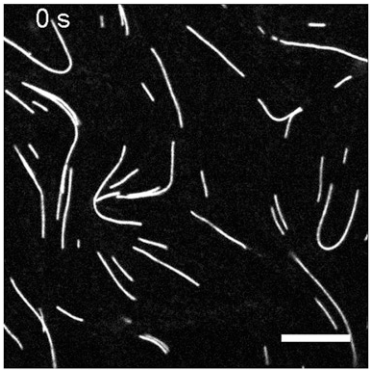

Movie S13. F-actin does not sever spontaneously due to high exposure. Shown are images of F-actin labeled with Alexa 568 (0.03 μM) in a network of dark F-actin (1.0 μM) and crowded to the surface of a 91% EPC/9% NTA bilayer by 0.25% MC. Images are taken every 5 s for 182 frames (910 s total). (Scale bar, 10 μm.) (Fig. S10*B*.)

Movie S13

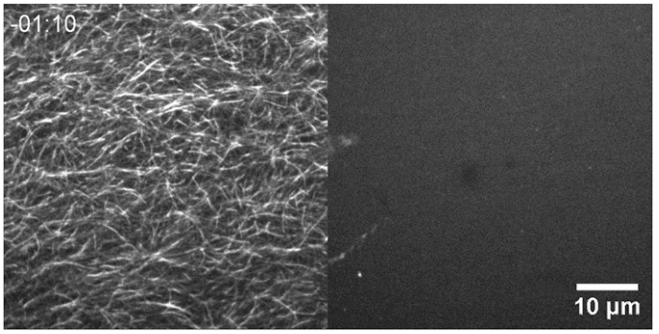

Movie S14. Contraction of adherent network (R_{xlink} = 0, R_{Adh} = 10). (*Left*) Images of F-actin (~1.32 μM) labeled with Alexa 568 crowded to the surface of a 91% EPC/9% NTA bilayer incubated with 10 μM of His-FimA2 (R_{Adh} = 10). (*Right*) Skeletal muscle myosin II (50 nM) labeled with Alexa 647 assembles at 00:00. Time is in min:s.

Movie S14